Geophys. J. Int. (2009) doi: 10.1111/j.1365-246X.2009.04326.x

Contribution of gravitational potential energy differences to the global stress field

Attreyee Ghosh,[1] William E. Holt,[2] and Lucy M. Flesch[3]

[1]*Department of Earth Science, University of Southern California,* CA 90059*, USA. E-mail: attreyg@usc.edu*
[2]*Department of Geosciences, Stony Brook University, Stony Brook,* NY 11794-2100*, USA*
[3]*Department of Earth and Atmospheric Sciences, Purdue University, West Lafayette,* IN 47907*, USA*

Accepted 2009 July 6. Received 2009 June 26; in original form 2009 January 10

SUMMARY

Modelling the lithospheric stress field has proved to be an efficient means of determining the role of lithospheric versus sublithospheric buoyancies and also of constraining the driving forces behind plate tectonics. Both these sources of buoyancies are important in generating the lithospheric stress field. However, these sources and the contribution that they make are dependent on a number of variables, such as the role of lateral strength variation in the lithosphere, the reference level for computing the gravitational potential energy per unit area (GPE) of the lithosphere, and even the definition of deviatoric stress. For the mantle contribution, much depends on the mantle convection model, including the role of lateral and radial viscosity variations, the spatial distribution of density buoyancies, and the resolution of the convection model. GPE differences are influenced by both lithosphere density buoyancies and by radial basal tractions that produce dynamic topography. The global lithospheric stress field can thus be divided into (1) stresses associated with GPE differences (including the contribution from radial basal tractions) and (2) stresses associated with the contribution of horizontal basal tractions. In this paper, we investigate only the contribution of GPE differences, both with and without the inferred contribution of radial basal tractions. We use the Crust 2.0 model to compute GPE values and show that these GPE differences are not sufficient alone to match all the directions and relative magnitudes of principal strain rate axes, as inferred from the comparison of our depth integrated deviatoric stress tensor field with the velocity gradient tensor field within the Earth's plate boundary zones. We argue that GPE differences calibrate the absolute magnitudes of depth integrated deviatoric stresses within the lithosphere; shortcomings of this contribution in matching the stress indicators within the plate boundary zones can be corrected by considering the contribution from horizontal tractions associated with density buoyancy driven mantle convection. Deviatoric stress magnitudes arising from GPE differences are in the range of 1–4 TN m^{-1}, a part of which is contributed by dynamic topography. The EGM96 geoid data set is also used as a rough proxy for GPE values in the lithosphere. However, GPE differences from the geoid fail to yield depth integrated deviatoric stresses that can provide a good match to the deformation indicators. GPE values inferred from the geoid have significant shortcomings when used on a global scale due to the role of dynamically support of topography. Another important factor in estimating the depth integrated deviatoric stresses is the use of the correct level of reference in calculating GPE. We also elucidate the importance of understanding the reference pressure for calculating deviatoric stress and show that overestimates of deviatoric stress may result from either simplified 2-D approximations of the thin sheet equations or the assumption that the mean stress is equal to the vertical stress.

Key words: Continental margins: convergent; Continental margins: divergent; Continental margins: transform; Dynamics of lithosphere and mantle; Dynamics: gravity and tectonics; Neotectonics.

1 INTRODUCTION

Since the advent of plate tectonics there have existed considerable controversies regarding the nature, magnitude and source of the forces that drive tectonic plates. The lithospheric stress field serves as an important indicator of these plate-driving forces. Lateral density variations

within the lithosphere have been shown to be a major factor influencing the global stress field (Frank 1972; Artyushkov 1973; Fleitout & Froidevoux 1982, 1983; Fleitout 1991; Coblentz *et al.* 1994; Coblentz & Sandiford 1994; Sandiford & Coblentz 1994; Coblentz *et al.* 1995; Iaffaldano *et al.* 2006). Lithospheric deformation is not confined along narrow plate boundaries. Rather, deformation within many plate boundary zones is distributed (McKenzie 1972; Molnar & Tapponnier 1975; England & McKenzie 1982; Molnar 1988; England & Jackson 1989; England & Molnar 1997; Flesch *et al.* 2000), with the bulk of crustal strain accommodated along major fault zones (Holt & Haines 1995; Holt *et al.* 2000; Thatcher 2007; Meade 2007). In present-day modelling of the tectonic stresses, the notion of rigid plates has been replaced by the notion of the continental lithosphere behaving as a continuous medium (England & Jackson 1989). The importance of this is the recognition that resulting crustal thickening and thinning leads to important internal lateral and vertical density variations; these lateral and vertical variations profoundly influence the deviatoric stress field in the lithosphere. Furthermore, it has also been recognized that horizontal dimensions of deformation far exceed the thickness of the lithosphere, and in this regard lithospheric deformation has been quantified in terms of a thin viscous sheet to solve for the depth averaged or depth integrated deviatoric stresses within the lithosphere over large scales (England & McKenzie 1982; Houseman & England 1986; England & Jackson 1989; England & Molnar 1997; Flesch *et al.* 2001; Ghosh *et al.* 2006, 2008). The assumption that goes with the thin sheet approximation is that the gradients of shear tractions at the base of the plate are negligibly small compared to the force of gravity acting on density.

In terms of a thin sheet approach, the sources of stress within the lithosphere can be divided into two main categories: (1) stresses associated with differences in gravitational potential energy per unit area (GPE differences) and (2) stresses associated with horizontal tractions. Note that gravity acting on density buoyancies below the lithosphere can lead to both radial and horizontal tractions. The radial tractions can lead to dynamic topography. We define GPE as the depth integrated vertical stress from surface of variable topography down to a common-depth reference level. Therefore, the GPE contribution can contain the contribution from radial tractions associated with density buoyancy-driven convection, since present-day topography contains, in places, a component of topography that may have a dynamic origin. Removing the inferred dynamic component from the GPE differences involves compensating the lithosphere model via elevation adjustment. In this paper, we use the thin sheet approximation to quantify deviatoric stresses within the lithosphere that are associated with GPE differences, both with and without the inferred contribution from dynamic topography.

Generally, our depth of integration is from the surface down to a constant reference level of 100 km below sea level. This incorporates the lithosphere for most parts of the Earth. However, we do investigate one special case of the contribution from deeper continental keels. Under the assumption that there is no buoyancy-driven mantle convection, no dynamic topography, and hence, equal vertical stress at the depth of the deepest continental keels, we integrate to a greater depth to account for deeper density buoyancies associated with continental keels. Although neglecting the above factors represents an oversimplified approximation, we nevertheless explore the influence of integrating to the base of the deepest continental keels to quantify differences with our standard reference level of 100 km.

We also investigate the role of lateral strength variations in the lithosphere. We calculate the depth integrated deviatoric stresses on a one-plate planet of uniform lithospheric viscosity, in addition to the more realistic stress calculations on an Earth-like planet with weak plate boundaries. We show how the consideration of laterally variable viscosities in the lithosphere enable the calculated deviatoric stresses to have a better match with stress and strain rate observations.

Calculation of GPE requires a level of reference. When the vertical stress is laterally variable at the base of the depth of integration, the choice of reference level has important dynamic implications. In this paper, we discuss the reference level problem in calculating GPE, and show that for a thin sheet calculation in which the vertical stress varies beneath topography along the base of the depth of integration, there is only one correct level of reference. In particular, we show that for such cases, the shallow density anomalies have a more dominant effect on the depth integrated deviatoric stresses than the deeper anomalies. Another important aspect of our study is to bring forward substantial changes in stress magnitudes that arise by solving the full 3-D force-balance equations instead of the 2-D equations, and also the importance of using a correct definition of deviatoric stress. Although the total forces driving lithospheric deformation are a combination of both GPE differences (including contribution from radial tractions) and horizontal tractions arising from density buoyancy-driven mantle convection (Lithgow-Bertelloni & Guynn 2004), our study focuses only on quantification of the GPE contribution. We have addressed the contribution from horizontal tractions elsewhere (Ghosh *et al.* 2008). Our confidence in the magnitude and distribution of GPE variations exceeds our confidence in the magnitude and direction of basal tractions associated with mantle convection. Nevertheless, if the contribution from GPE differences can be correctly quantified, both with and without inferred dynamic topography, then the misfit of the associated depth integrated deviatoric stress field with stress tensor indicators holds promise for constraining the contribution associated with horizontal basal tractions. Therefore, it is important to isolate the contribution of GPE differences to depth integrated deviatoric stresses because they calibrate the absolute magnitudes of deviatoric stresses acting within the lithosphere.

2 THE FORCE BALANCE EQUATIONS AND VALIDITY OF THE THIN SHEET APPROXIMATION

The force balance equations, which state that gradients of stresses are balanced by the force of gravity per unit volume, are given by

$$\frac{\partial \sigma_{ij}}{\partial x_j} + \rho g_i = 0, \tag{1}$$

where σ_{ij} is the ijth component of the total stress tensor, x_j is the jth coordinate axis, ρ is the density and g_i is the ith component of the acceleration due to gravity (England & Molnar 1997). The above equations use summation notation, where i takes the values of x, y and z and

the repeated index j represents the summation over x, y and z. For clarity we show the cartesian form of (1). However, we solve the spherical form of (1) in our global calculations (see Appendix A).

We now explore the conditions under which the thin sheet approximation is valid. The basis of the thin sheet approach is that because the horizontal distance scales are large in comparison with the thickness of the lithosphere, we can compute depth integrals of the force balance equations down to a constant reference level, and then solve these equations for the depth integrals of deviatoric stress within that layer. Expanding the z-equation from (1) and then integrating from the surface to the base of a uniform reference level, L, yields

$$\frac{\partial}{\partial x}\left[\int_{-h}^{L}\sigma_{xz}(z)dz\right]+\frac{\partial}{\partial y}\left[\int_{-h}^{L}\sigma_{yz}(z)dz\right]+\frac{\partial}{\partial z}\left[\int_{-h}^{L}\sigma_{zz}(z)dz\right]=-\int_{-h}^{L}\rho g_z dz. \tag{2}$$

The approximation in the thin sheet approach is that

$$\frac{\partial}{\partial x}\int_{-h}^{L}\sigma_{xz}(z)dz+\frac{\partial}{\partial y}\int_{-h}^{L}\sigma_{yz}(z)dz << -\int_{-h}^{L}\rho g_z dz, \tag{3}$$

such that, from (2) we have

$$\sigma_{zz}(z)=-\int_{-h}^{z}\rho g(z')dz'. \tag{4}$$

Assuming that $\sigma_{xz}(z)$ and $\sigma_{yz}(z)$ are linear, from zero at the surface to $\sigma_{xz}(L)$ and $\sigma_{yz}(L)$ at the base, L, then the question is how large can the gradients of shear tractions be in order for (3) to hold ? Using 3000 kg m^{-3} for an average density of the lithosphere and a 100 km thick lithosphere, we find that horizontal gradients in shear tractions applied to the base of the lithosphere at a depth of 100 km would have to be as high as 6 MPa/10 km for the left-hand side of (3) to be 1 per cent of the magnitude of the right-hand side of (3), the vertical stress at depth L. This is at least an order of magnitude higher than horizontal variations of tractions from large scale mantle circulation (Steinberger *et al.* 2001; Becker & O'Connell 2001), and is likely to be much larger than the most extreme gradients in tractions that might occur beneath subduction zones. Therefore, the 'thin sheet' approximation in (3) is valid, in which case we can use the relation in (4) for the vertical stress, and solve only the two horizontal force balance equations to investigate depth integrals of horizontal deviatoric stress.

Substituting into (1) for the total stresses via the relationship, $\tau_{ij}=\sigma_{ij}-\frac{1}{3}\sigma_{kk}\delta_{ij}$, where τ_{ij} is the ijth component of the deviatoric stress tensor, δ_{ij} is the Kronecker delta, and $\frac{1}{3}\sigma_{kk}$ is the mean total stress and integrating (1) over the thickness of the lithosphere, we arrive at the full horizontal force balance equations, neglecting flexure (England & McKenzie 1982; England & Houseman 1986; England & Molnar 1997; Flesch *et al.* 2001):

$$\frac{\partial\bar{\tau}_{xx}}{\partial x}-\frac{\partial\bar{\tau}_{zz}}{\partial x}+\frac{\partial\bar{\tau}_{xy}}{\partial y}=-\frac{\partial\bar{\sigma}_{zz}}{\partial x}+\tau_{xz}(L) \tag{5}$$

$$\frac{\partial\bar{\tau}_{yx}}{\partial x}+\frac{\partial\bar{\tau}_{yy}}{\partial y}-\frac{\partial\bar{\tau}_{zz}}{\partial y}=-\frac{\partial\bar{\sigma}_{zz}}{\partial y}+\tau_{yz}(L), \tag{6}$$

where the over bars represent depth integration. The terms on the right-hand sides of eqs (5) and (6) constitute body-force-like terms, the first terms representing horizontal gradients in GPE per unit area, and $\tau_{xz}(L)$ and $\tau_{yz}(L)$ representing tractions, arising from density buoyancy-driven mantle convection, applied at the base of the thin sheet at depth L. We do not quantify the contributions of $\tau_{xz}(L)$ and $\tau_{yz}(L)$ here, but have addressed them elsewhere (Ghosh *et al.* 2008).

The thin sheet approximation also implicitly assumes that vertical variations in horizontal velocity are small, or that one of the principal axes of the stress or strain rate tensor is close to vertical. The presence of a basal traction boundary condition in (5) and (6), associated with a deeper mantle density buoyancy contribution, calls for the need to evaluate the validity of this assumption. If one principal axis is close to vertical, then depth integrals of shear stress should be small in comparison with depth integrals of horizontal deviatoric stress. Using 5 MPa for $\sigma_{xz}(L)$, and assuming a linear gradient of $\sigma_{xz}(L)$, such that it is zero at the surface, the depth integrals of $\sigma_{xz}(z)$ are 2.5×10^{11} N m^{-1}. This is about 10 per cent of the magnitude of the depth integral of horizontal deviatoric stress in the lithosphere (Ghosh *et al.* 2008). Therefore, even in the presence of basal tractions of significant magnitude, the assumption that one of the principal axes is near-vertical appears to be valid.

The forcing terms in (5) and (6) are constrained by observations. For example, GPE per unit area is constrained by topography and seismically defined crustal thicknesses (Crust 2.0 [G. Laske *et al.*, Crust 2.0: A new global crustal model at 2 × 2 degrees, 2002, available at http://mahi.ucsd.edu/Gabi/rem.html]) and tractions can be constrained by self-consistent circulation models that match plate motions, dynamic topography and geoid (e.g. Wen & Anderson 1997). Depth integration over the entire plate thickness is indicated by bars over the total stress and deviatoric stress terms, σ_{ij} and τ_{ij}, respectively. The vertically integrated vertical stress, $\bar{\sigma}_{zz}$, which is the negative of GPE per unit area is given by

$$\bar{\sigma}_{zz}=-\int_{-h}^{L}\left[\int_{-h}^{z}\rho(z')g dz'\right]dz=-\int_{-h}^{L}(L-z)\rho(z)g\,dz \tag{7}$$

based on a reference level of depth L (Jones *et al.* 1996). Here, $\rho(z)$ is the density, L is a constant depth base of thin sheet, h is the topographic elevation and g is the acceleration due to gravity.

3 METHOD FOR SOLVING THE FORCE BALANCE EQUATIONS

The deviatoric stress field solution that we obtain is the mathematically unique solution that both balances the body force distribution (GPE differences) and provides a global minimum in the second invariant of stress [following Flesch *et al.* (2001)]. We also take into account weak plate boundaries and strong plates, as discussed further. Solutions to (5) and (6) for $\bar{\tau}_{ij}$ can be obtained, given distributions of $\frac{\partial \bar{\sigma}_{zz}}{\partial x}$ and $\frac{\partial \bar{\sigma}_{zz}}{\partial y}$ with $\tau_{xz}(L)$ and $\tau_{yz}(L)$ set to zero (e.g. Flesch *et al.* 2001; Ghosh *et al.* 2006). Alternatively, solutions can be obtained given distributions of $\tau_{xz}(L)$, $\tau_{yz}(L)$, with gradients in GPE set to zero. The contribution from basal tractions can simply be added to the contribution from GPE differences to obtain the full stress field (Ghosh *et al.* 2008). This motivates our study to correctly quantify the global solution associated with GPE distribution to better understand the full global solution that has contributions from density variations at all depths.

Previously, most authors had used the geoid surface (sea level) as the reference level for calculating GPE (Fleitout 1991; Coblentz *et al.* 1994; Jones *et al.* 1996; Zoback & Mooney 2003), in which case,

$$\bar{\sigma}_{zz}{}' = \int_{-h}^{L} \rho(z) g z \, dz = \bar{\sigma}_{zz} + L\sigma_{zz}(L). \tag{8}$$

Thus, for areas in which $\sigma_{zz}(L)$ is a constant, the choice of reference level is irrelevant (Haxby & Turcotte 1978). However, this reference level yields significantly different values from that obtained using (7) when the pressure, $\sigma_{zz}(L)$, at the reference level L is non-uniform, as we discuss in a later section. We use both the Crust 2.0 model and the EGM96 geoid model (available from NIMA at http://164.214.2.59/GandG/wgs-84/egm96.html) to calculate GPE. We show that the latter can only be used as a proxy for GPE if the pressure or vertical stress at the base of the layer of integration is globally uniform.

We use a finite element method (described further) to solve the 3-D force balance equations over a global grid of $2.5^\circ \times 2.5^\circ$ for the spherical case, neglecting horizontal basal tractions, to quantify the contributions to deviatoric stresses arising from GPE differences. We minimize the functional (after Flesch *et al.* 2001):

$$I = \int_S \frac{1}{\mu}[\bar{\tau}_{\alpha\beta}\bar{\tau}_{\alpha\beta} + \bar{\tau}_{\gamma\gamma}^2]\mathrm{d}S + \int_S 2\lambda_\alpha \Big[\frac{\partial}{\partial x_\beta}(\bar{\tau}_{\alpha\beta} + \delta_{\alpha\beta}\bar{\tau}_{\gamma\gamma}) + \frac{\partial \bar{\sigma}_{zz}}{\partial x_\alpha}\Big]\mathrm{d}S, \tag{9}$$

where μ is the relative viscosity, $\bar{\tau}_{\alpha\beta}$ is the vertically integrated horizontal deviatoric stress, $\bar{\tau}_{\gamma\gamma} = \bar{\tau}_{xx} + \bar{\tau}_{yy}$, λ_α is the horizontal component of the Lagrange multiplier for the constraint to satisfy the two force balance differential equations, $\bar{\sigma}_{zz}$ is the vertically integrated vertical stress (GPE per unit area) and S represents area of the entire Earth's surface. In Flesch *et al.* (2001), μ was assigned a value of 1. We assign variable values to μ to approximate weak plate boundary zones and strong plates. This is done in two ways. In the first case, an inverse relationship between strain rates (from Kreemer *et al.* 2003) and relative viscosities, μ, is assumed (Fig. 1a). The relative viscosities of the deforming plate boundary regions are obtained by assigning a reference viscosity to the moderately straining region in western North America with a strain rate of $1.5 \times 10^{-7}\,\mathrm{yr}^{-1}$ via the relationship:

$$\frac{1}{\mu} = 1 + \left(\frac{1}{\mu_{\mathrm{ref}}} - 1\right)\sqrt{\frac{E^2}{E_{\mathrm{ref}}^2}}, \tag{10}$$

where μ_{ref} is the viscosity corresponding to the above-mentioned area, $E^2 = 2(\dot{\epsilon}_{xx}^2 + \dot{\epsilon}_{yy}^2 + \dot{\epsilon}_{xy}^2 + \dot{\epsilon}_{xx}\dot{\epsilon}_{yy})$, where $\dot{\epsilon}_{xx}$, $\dot{\epsilon}_{yy}$ and $\dot{\epsilon}_{xy}$ are strain rates from Kreemer *et al.* (2003), and E_{ref}^2 is the reference value for E^2, corresponding to the value for μ_{ref}. The lowest viscosities occur along the mid-oceanic ridges, whereas relatively higher viscosities occur in the deforming continental areas (Fig. 1a). The rigid plates (blank regions) have the highest viscosities with a μ value of 1. We test different values for the reference viscosity, μ_{ref}, such as 1/3, 1/30, 1/300 and 1/3000, where the reference region in western North America is 3, 30, 300 and 3000 times weaker than the plates, respectively. The viscosity structure giving rise to the deviatoric stress field that matches the deformation indicators best is chosen. Taking into account the above viscosity variations yields a focusing of stresses within the plates and fits well the observed SH_{max} orientations in most places within the plates (Zoback 1992).

The second way takes into account the dependence of effective viscosities on lithospheric thickness in addition to strain rates (Fig. 1b). The viscosity, μ', in this case is given by

$$\mu' = \frac{1}{100}\int_{-h}^{L'} \mu dz = \frac{1}{100}(L' + h)\mu, \tag{11}$$

where $L' + h$ is the thickness of the lithosphere and μ are the strain rate dependent viscosities. We consider both types of viscosities (eqs 10 and 11) in our models. However, all the figures are based on viscosities using the first method (Fig. 1a). Note that here L' is no longer constant; the variable base of the lithosphere is taken into account. In the case where GPE is calculated with a reference level of 100 km, the maximum value of L' is fixed at 100 km. Therefore, in this case, our depth integrals do not encompass the deeper lithospheric keels, but take into account the variable depths of the oceanic lithosphere. However, we do address a case where $L' = 270$ km, a depth great enough to include the keels. Note, in (11), the lithosphere thickness is normalized by a reference thickness of 100 km. Areas deforming at the same rate will have different viscosities based on lithospheric thickness: thicker lithosphere will be stronger than lithosphere that is less thick.

We minimize (9) with respect to $\bar{\tau}_{\alpha\beta}$ using the variational principle (Morse & Feshbach 1953), which then yields the relation

$$\bar{\tau}_{\alpha\beta} = \frac{1}{2}\left(\frac{\partial \lambda_\alpha}{\partial x_\beta} + \frac{\partial \lambda_\beta}{\partial x_\alpha}\right), \tag{12}$$

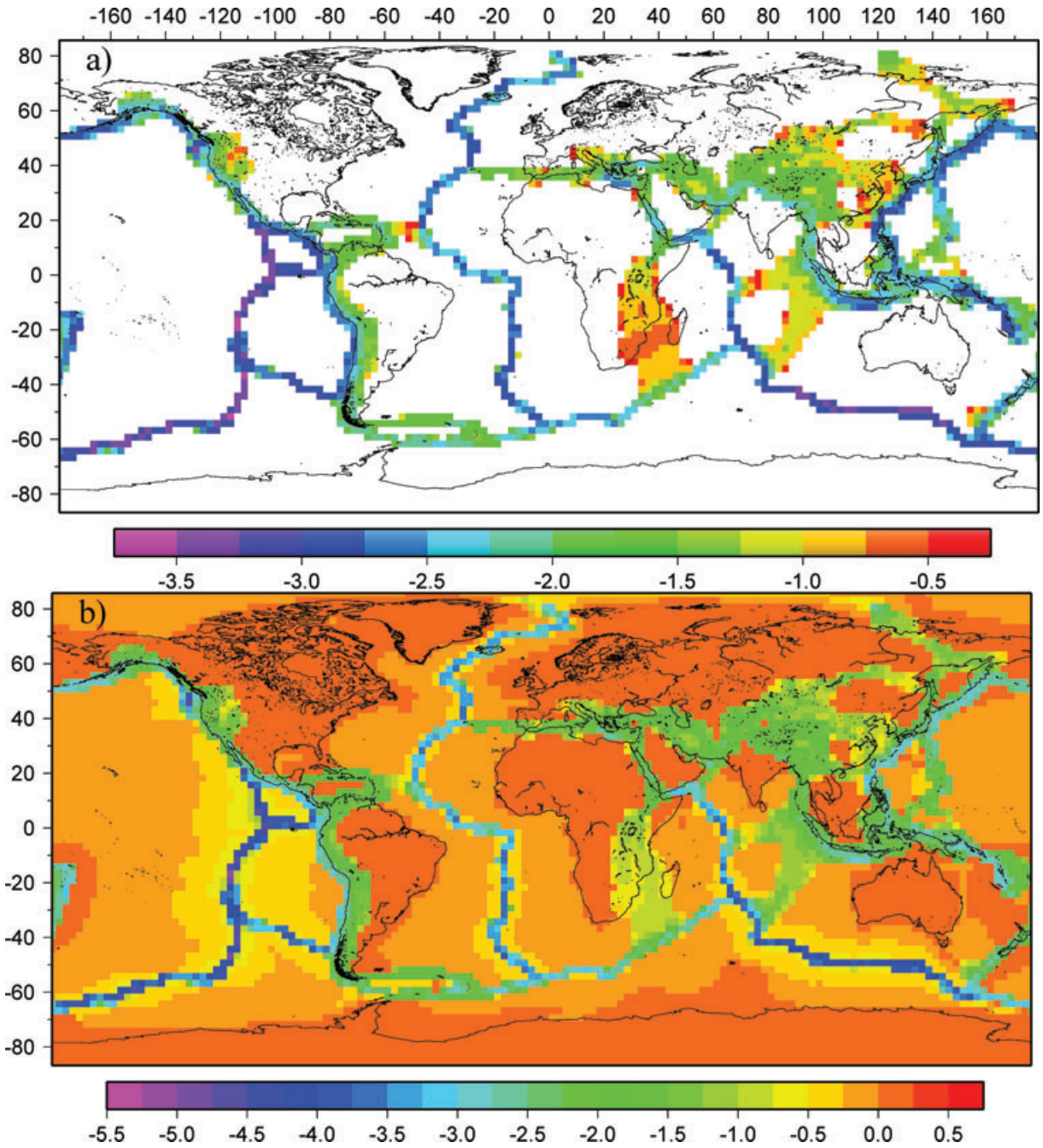

Figure 1. Logarithm of relative viscosity distribution for all the plates based on (a) strain rates from GSRM and (b) both strain rates and lithospheric thickness. The white areas represent intra-plate regions with relative viscosity 1. A reference viscosity of $\mu_{\rm ref} \sim \frac{1}{30}$ is chosen at the moderately fast straining western North America (1.5×10^{-7} yr^{-1}). Areas with higher viscosities than $\mu_{\rm ref}$ are deforming at a slower rate.

where $\bar{\tau}_{\alpha\beta}$ has the same relation with the vector of Lagrangian multipliers as does the strain rate, $\dot{\epsilon}_{\alpha\beta}$, to the velocity vector. Substituting $\bar{\tau}_{\alpha\beta}$ from (12) into the J functional below (Flesch *et al.* 2001) and then minimizing the functional J with respect to the Lagrange multipliers yields the force balance equations that the Lagrange multipliers have to satisfy.

$$J = \int_S \left[\begin{pmatrix} \bar{\tau}_{xx} \\ \bar{\tau}_{yy} \\ \bar{\tau}_{xy} \end{pmatrix} - \begin{pmatrix} \Phi^{\rm obs}_{xx} \\ \Phi^{\rm obs}_{yy} \\ \Phi^{\rm obs}_{xy} \end{pmatrix} \right]^T \widetilde{V}^{-1} \left[\begin{pmatrix} \bar{\tau}_{xx} \\ \bar{\tau}_{yy} \\ \bar{\tau}_{xy} \end{pmatrix} - \begin{pmatrix} \Phi^{\rm obs}_{xx} \\ \Phi^{\rm obs}_{yy} \\ \Phi^{\rm obs}_{xy} \end{pmatrix} \right] {\rm d}S, \tag{13}$$

where $\bar{\tau}_{xx}$, $\bar{\tau}_{yy}$ and $\bar{\tau}_{xy}$ are the vertically integrated deviatoric stresses that we are solving for, $\widetilde{V}^{-1}$ is the covariance matrix (see Appendix A), and $\Phi^{\rm obs}_{xx} = \Phi^{\rm obs}_{yy} = -\frac{1}{3}\bar{\sigma}_{zz}$ and $\Phi^{\rm obs}_{xy} = 0$ are potentials whose spatial derivatives involve body force equivalent terms. Minimizing J with respect to the Lagrange multipliers provides a unique solution to the force balance equations that corresponds to the global minimum in the

second invariant of deviatoric stress (e.g. the functional in (9) is also optimized (Flesch *et al.* 2001)). The methodology of minimizing J in (13) is analogous to solving the Weak formulation of the linear viscous problem, with generally laterally variable linear viscosity, where the Lagrange multipliers in (12) hold the mathematical equivalence with velocity. The basis functions for the Lagrange multipliers are higher order elements on the $2.5^\circ \times 2.5^\circ$ square grid involving the Bessel form of bi-cubic spline interpolation (de Boor 1978; Beavan & Haines 2001) and $\lambda_\alpha = \lambda_\beta = 0$ on the boundary ∂S. This boundary is defined as two ring segments: one at 88°S and one at 87°N.

A full benchmarking exercise using this finite element methodology is described in the supplementary appendix of Ghosh *et al.* (2008), where they have recovered the horizontal components of the deviatoric stress field associated with full degree 12 3-D convection models for the globe. The full 3-D convection model has the long-wavelength components of 3-D flow in all of the present-day subduction zones. Ghosh *et al.* (2008) show that the finite element method can recover these stress fields given only the body force equivalent terms from the full 3-D model; it is not necessary to know the absolute viscosity magnitudes used in the 3-D convection models to recover stresses using this finite element method. The body force equivalent terms derived from the 3-D convection model, and then separately applied in the thin sheet finite element model, are the depth integrated vertical stresses, or GPE, including the contribution from dynamic topography and the horizontal traction output at the reference level, L (see Ghosh *et al.* 2008). Similarly, Klein *et al.* (2009) have shown that if the relative viscosity variations are known, then the exact deviatoric stress field can be recovered given known body force equivalents.

4 GPE FROM CRUST 2.0

We use the crustal thicknesses and densities from the Crust 2.0 model to calculate GPE per unit area. For the oceanic regions, we use the cooling plate model based on ocean floor age data (Müller *et al.* 1997) and with revised parameters from Stein & Stein (1992) to define densities there. Beneath the continental lithosphere, the densities of the last layer of the crustal model are replaced by an upper-mantle density of 3300 kg m^{-3}. The reference level, L, is chosen as 100 km (after Jones *et al.* 1996) in this particular case. Where no seafloor age data are provided, the densities were not adjusted and the original Crust 2.0 model densities, together with the model crustal thickness and elevation data, were used to define GPE. We also use a deeper reference level to take into account the density buoyancies associated with cratonic roots, which we discuss in a later section. Because water and ice are unable to transmit significant tectonic shear stresses, effects of ice and water layers are excluded from our GPE calculation. However, we take into account the pressure exerted by water and ice layers that constitutes a boundary condition in the computation of the GPE integral (eq. 7). The GPE calculated from crustal thickness estimates of Crust 2.0 show high values occurring at high elevation regions like the Andes, western North America, eastern Africa, Tibetan plateau, as well as at the mid-oceanic ridges, with the maximum GPE occurring at the Tibetan plateau (Figs 2 and C1a). Lower elevation regions like the ocean basins and topographically low continental areas exhibit low GPE. The resultant depth integrated deviatoric stress magnitudes show a maximum depth integral of deviatoric tension at the Tibetan plateau ($\sim 2 \times 10^{12}$ N m^{-1}) (Fig. C1a) and compressional deviatoric stresses in the older oceans and low elevation continental regions ($\sim$1–1.5 $\times 10^{12}$ N m^{-1}). The mid-oceanic ridges are in deviatoric tension as are

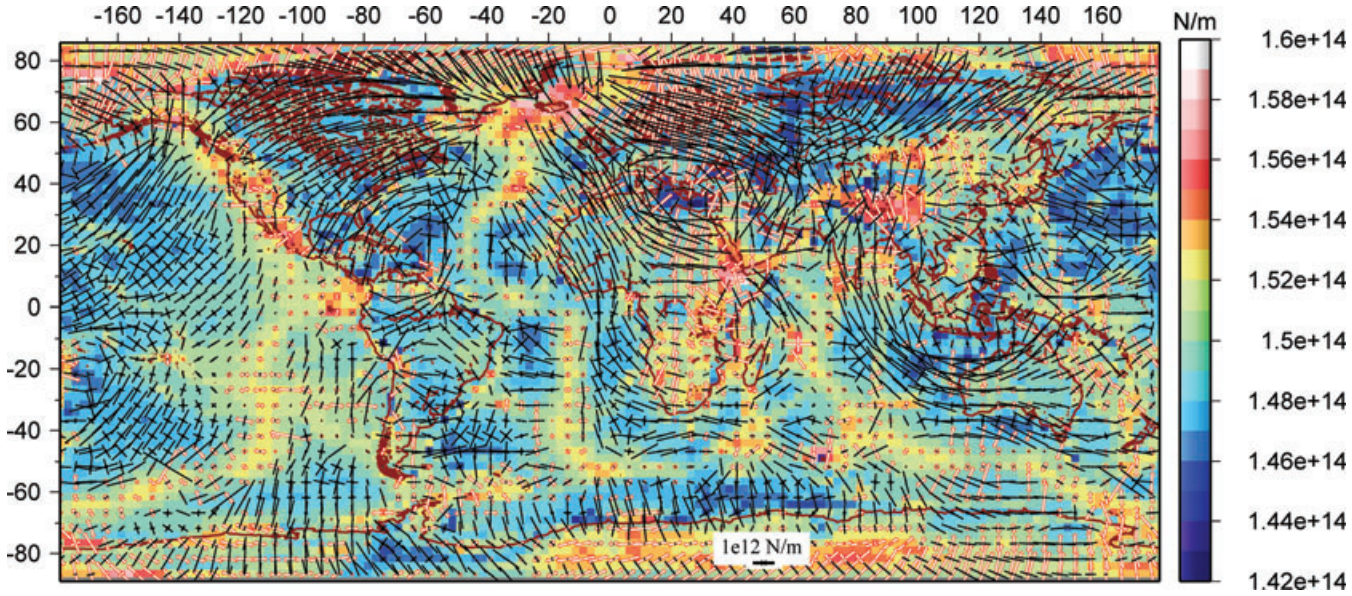

Figure 2. Global distribution of vertically integrated horizontal deviatoric stresses and GPE calculated from the uncompensated Crust 2.0 model. Tensional deviatoric stresses are shown by red arrows whereas compressional deviatoric stresses are shown by black arrows. Length of the arrows are proportional to the magnitude of stresses. Strike-slip regions are indicated by one tensional and one compressional pair of arrows. Areas having high GPE are in deviatoric tension whereas areas having low GPE are in deviatoric compression. GPE on scalebar is in Newton metre^{-1} and corresponds to the depth integral of σ_{zz} from the Earth's surface to the reference level L at 100 km below sea level.

topographically high areas that have higher GPE values. Moreover, the depth integrated deviatoric stresses for the Indo-Australian plate agree with the SH_{max} directions of the WSM (Zoback 1992; Reinecker *et al.* 2005) and those derived by Sandiford *et al.* (1995). Western North America is dominated by tensional stresses whereas the rest of the continent east of the Rocky Mountains undergoes deviatoric compression (Figs 2 and C1b). The Aegean region is dominated by strike-slip style of deformation (Fig. C1c). The stress pattern in the Central Indian Ocean region (Fig. C1d) exhibits a rotation of the axes that matches the stress observations from the WSM in that region (Zoback 1992; Reinecker *et al.* 2005). The stresses in eastern Africa show pure tension (Fig. C1e) with stress magnitudes decreasing southward.

It should be noted that the GPE values, and the deviatoric stresses, of the low elevation portions of old continents and old oceans are similar (Fig. 2). This is because GPE is a function of both elevation and density. Although the continents have a greater elevation than the oceans, the continental crust is in general less dense than the oceanic crust. Moreover, as the oceanic crust is thinner, a larger amount of denser mantle is included in the depth integral of vertical stress in oceanic lithosphere in comparison to the depth integral through continental lithosphere.

The above result for GPE and corresponding deviatoric stress solution is for an uncompensated Crust 2.0 model. That is, one interpretation of the variable pressure at the reference level, L, is that, in addition to the contribution from lithosphere buoyancies, this model encompasses the effect of radial tractions acting at the base of the lithosphere from deeper mantle density buoyancies. To investigate the effect of compensation, an isostatic solution was computed by compensating our model [equal pressure, $\int_{-h}^{L} \rho g dz = \sigma_{zz}(L)$, at the reference level L]. The concept of isostatic equilibrium dates back to the 19th century. The Airy model of isostatic compensation (Airy 1855) involves a constant density layer with variable thickness while the Pratt model (Pratt 1855) is based on a constant thickness layer of variable density. What occurs on Earth is possibly a combination of these two end-members, with different regions exhibiting each mechanism in varying degrees. The vertical stress at the reference level, L, given by

$$\sigma_{zz}(L) = \int_{-h}^{L} \rho(z) g \mathrm{d}z \tag{14}$$

can be equilibrated either by adjusting the density of the upper mantle, $\rho(z)$, or by adjusting the elevation, h, of the crustal blocks. In the latter case, the adjustment constitutes the removal of the inferred dynamic topography that has resulted from radial tractions applied at the reference level, L, [which is the inferred source of the variable values of $\sigma_{zz}(L)$].

Upper-mantle densities are adjusted with respect to an average vertical stress $\sigma_{zz}(L)$ for the continents and oceans. Although the resultant GPE differences and deviatoric stress solutions (Fig. 3) show values that are 10–20 per cent lower than the uncompensated case, the overall style of deviatoric tension and compression remain unchanged.

In the second method, compensation is achieved by adjusting the elevations based on an average vertical stress, $\sigma_{zz}(L)$, for the continents and oceans, while keeping the densities of the mantle unchanged. Thus, elevations of the crustal blocks are lowered or raised according to whether the actual vertical stress at reference level L is greater or less than the global average vertical stress there. Compensation by density adjustment does not acknowledge the existence of dynamic topography (discussed later), whereas in the latter case (Fig. 4), the entire deviation from constant pressure at the reference level, L, is assumed to be associated with dynamic topography. The deviatoric stress field in Fig. 4, therefore, represents the theoretical contribution of lithosphere buoyancies alone, with dynamic topography removed under the assumption that all variations in vertical stress at the reference level are due to dynamic topography. What occurs on Earth is a combination of these two

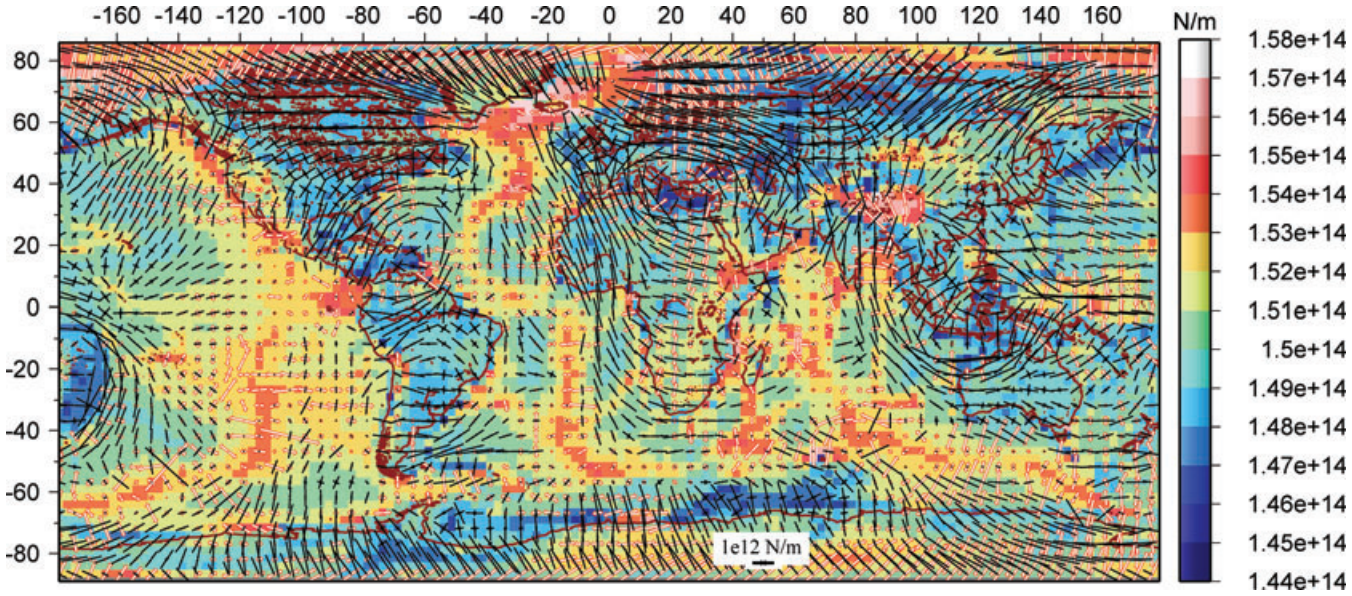

Figure 3. Global distribution of vertically integrated horizontal deviatoric stresses and GPE calculated from Crust 2.0, compensated by density adjustment. The range of GPE values, as well as the absolute magnitudes of deviatoric stresses, decrease compared to the uncompensated (in Fig. 2) case, but the overall pattern remains similar to that in Fig. 2.

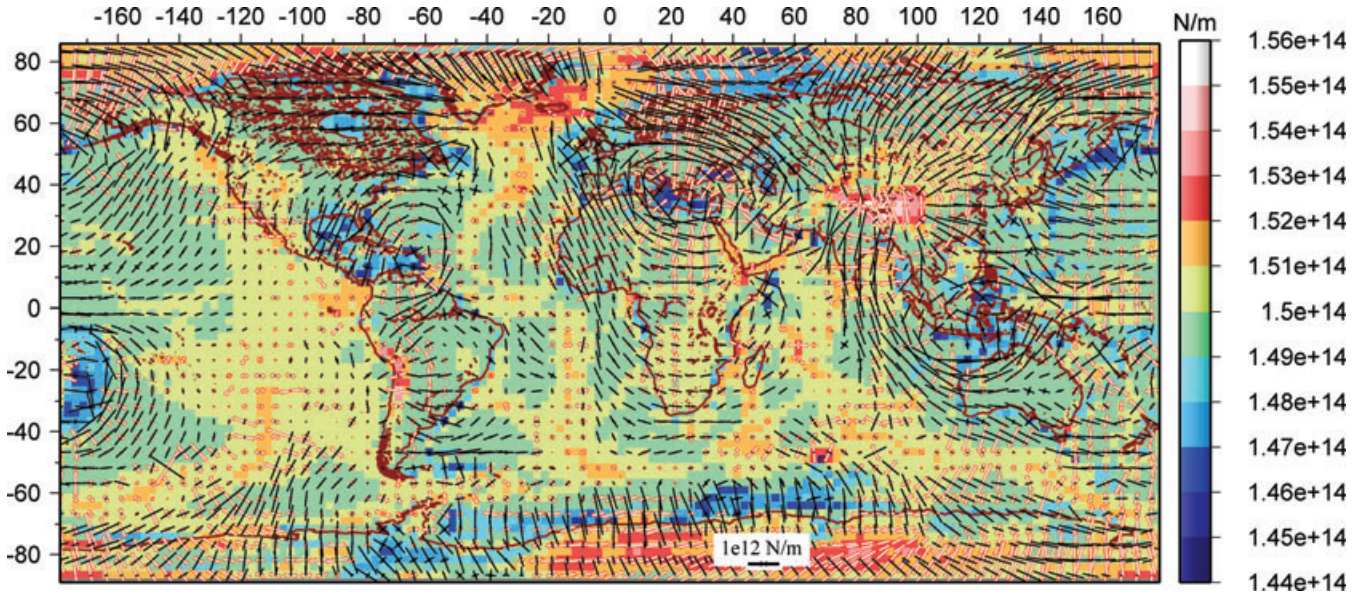

Figure 4. Global distribution of vertically integrated horizontal deviatoric stresses and GPE calculated from Crust 2.0, compensated by elevation adjustment. The range of GPE values, as well as the absolute magnitudes of deviatoric stresses, decrease compared to the uncompensated (in Fig. 2) as well as the other compensated case (Fig. 3), but the overall pattern remains similar to that in Figs 2 and 3. Because compensation is achieved via elevation adjustment, Fig. 4 is the theoretical response of lithosphere from internal buoyancies, with the influence of dynamic topography removed. Therefore, the GPE differences for young versus old oceanic lithosphere in this model arise only from the elevation and density changes associated with lithospheric cooling.

end-members. On comparing the GPE differences and deviatoric stress magnitudes for the two compensated cases (Figs 3 and 4), we find that magnitudes of both are reduced considerably in the latter case (compensation by elevation adjustment), although the deviatoric stress patterns are similar. Due to increasing density moment as a function of mass anomalies considered at increasing distances away from the reference level, L, (discussed in detail in Section 7), near-surface densities have a greater impact on the change in GPE than do deeper density variations. This means that adjustment of elevation has a greater impact on GPE differences, and associated deviatoric stress magnitudes, than the adjustment of density in the mantle. Another way of interpreting this result is that, assuming flexure to be negligible at long wavelengths, if horizontal variations in $\sigma_{zz}(L)$ are inferred to be associated with mantle flow or dynamic support, then the resulting dynamic topography is a major factor contributing to lithospheric GPE differences and deviatoric stresses associated with these GPE differences (compare Figs 2 and 4).

As a way of investigating the role of weak plate boundaries, we also compute deviatoric stresses with a uniform lithospheric viscosity ($\mu = 1$ in eq. 9) based on an uncompensated Crust 2.0 model. The resultant deviatoric stresses (Fig. 5) have magnitudes similar to those in the uncompensated case. However, the plate boundaries, in this uniform viscosity case, have higher stresses as compared to the plate boundaries in all the other cases (cases with lateral viscosity variations). When compared with the uncompensated result with lateral viscosity variations (Fig. 2), the stress patterns appear similar in a few areas, but differ substantially in many regions, particularly in the continents. Furthermore, the arcuate feature of compressive deviatoric stresses throughout the Indo-Australian plate boundary regions (observed in the WSM) is only achieved when lateral viscosity variations in the lithosphere are taken into consideration (refer to Fig. C1d and compare with Fig. 5). Lateral strength variations, with weak zones corresponding to the location of today's plate boundary zones, and stronger zones corresponding to position of the plates, therefore, plays a profoundly important role in affecting the deviatoric stress field.

5 DEEPER LITHOSPHERIC DENSITY BUOYANCIES

As mentioned earlier, we perform depth integrals to 100 km that is sometimes assumed to approximate the boundary between the non-convecting lithosphere and the convecting mantle. However, the base of the lithosphere is variable in depth due to the presence of continental keels, depth variations for different aged oceans, etc. Accounting properly for this variable depth involves sophisticated methods that we do not attempt in this paper. One can approximate the influence of variable bottom lithosphere, however, by integrating down to a constant reference level, equal to the depth of the deepest lithosphere. However, this can only be achieved under the assumption that there is no buoyancy-driven mantle convection acting on the variable base of lithosphere, and no dynamic topography. This implies total compensation; that is, equal vertical stress at the depth of the reference level (bottom of the deepest lithosphere).

To take into account the effects of the deeper density buoyancies associated with the lithosphere, the reference level, L, is extended to a greater depth. Based on the lithospheric thickness model of Conrad & Lithgow-Bertelloni (2006), we take L to be at the depth of the

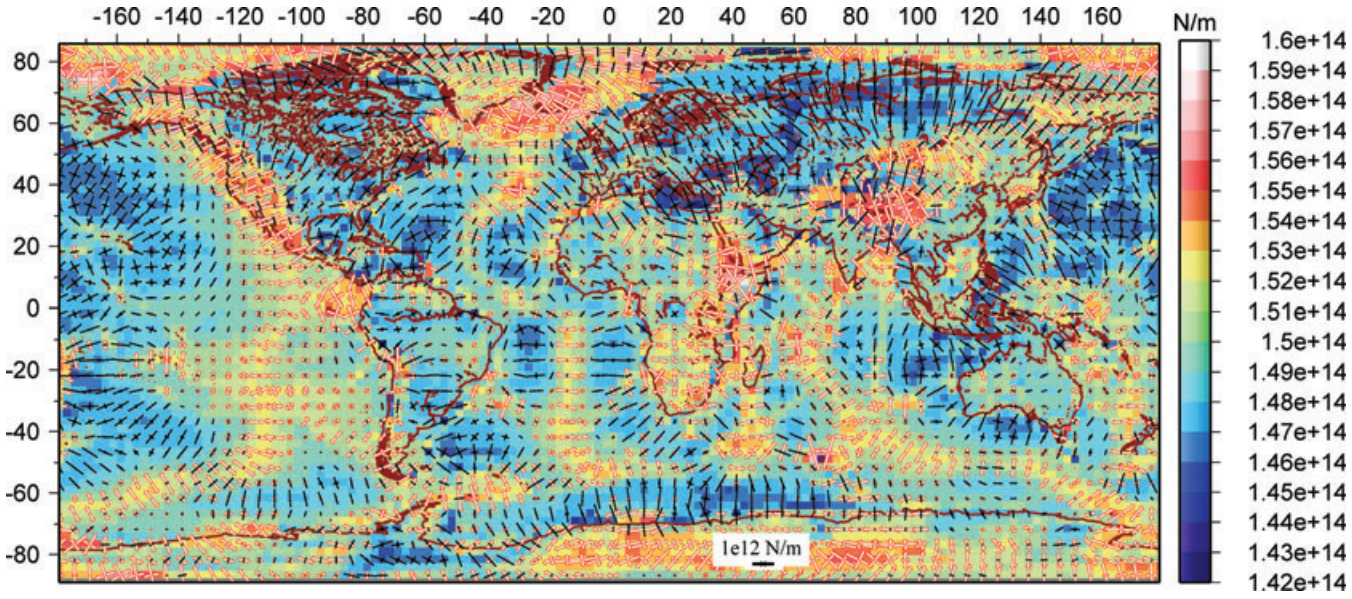

Figure 5. Same as Fig. 2, but with laterally uniform lithospheric viscosity. Note that significant changes occur in deviatoric stress orientations in many of the plate boundary zones (western North America, Mediterranean, Southeast Asia) as well as within the Indo-Australian plate region.

deepest lithosphere (∼270 km). Integrating to a depth of ∼270 km captures a significant portion of the asthenosphere. However, a constant asthenospheric density outside of the very deep cratonic areas makes no contribution to the deviatoric stress field.

To achieve compensation at L, we adjust the densities of the subcrustal layer (layer between the base of the crust and the base of the lithosphere) with respect to an average vertical stress at 270 km depth for continents and oceans. The asthenosphere layer (layer between the base of the lithosphere and the reference level, L) is assigned a constant density of 3300 kg m^{-3}. Based on these adjusted densities, the GPE and the corresponding deviatoric stress field are calculated with viscosities varying as a function of both strain rates (Fig. 1a) and combined strain rates and lithospheric thickness (Fig. 1b).

The absolute GPE values naturally increase when L is at a greater depth (Fig. 6). However, the GPE differences, and consequently the deviatoric stress magnitudes, are lower than the corresponding model compensated at 100 km (Fig. 3). The overall depth integrated deviatoric stress pattern in Fig. 6 is similar to the previous cases (Figs 2–4). The lower deviatoric stress magnitudes may indicate the influence of a lower density (less than 3300 kg m^{-3}) subcrustal lithospheric layer used in most of the regions to achieve compensation.

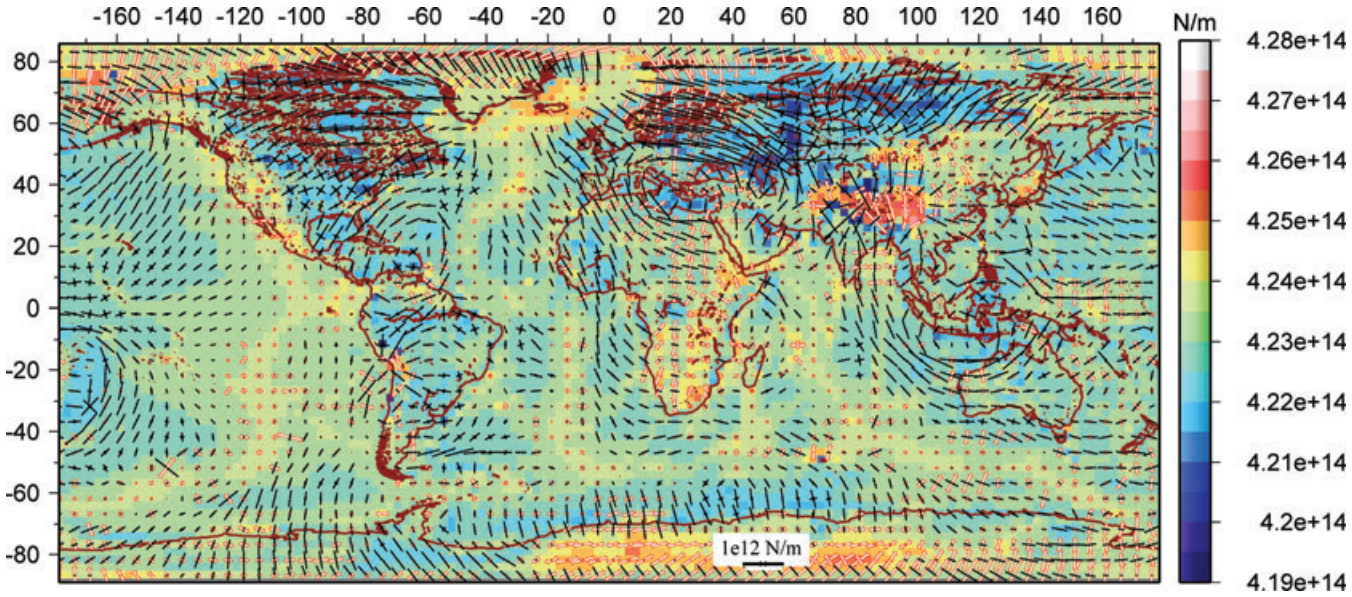

Figure 6. Same as Fig. 4, but compensated at the depth of the deepest lithosphere (∼270 km).

6 GPE FROM GEOID

We also calculate GPE from the EGM96 geoid data set. Geoid anomalies have been used to calculate GPE by Coblentz *et al.* (1994), Sandiford & Coblentz (1994), Flesch *et al.* (2000, 2001). Coblentz *et al.* (1994) calculated geoid anomaly as

$$\Delta N = -\frac{2\pi G}{g^2}\Delta U_l \tag{15}$$

where G is the universal gravitational constant, g is the acceleration due to gravity and ΔU is the GPE from geoid (given by (Turcotte & Schubert 1982))

$$\Delta U_l = -\int_0^L \Delta\rho(z) g z \, \mathrm{d}z = -\frac{\Delta N g^2}{2\pi G}. \tag{16}$$

However, this relationship is true only if isostatic compensation prevails everywhere at the reference level L (Haxby & Turcotte 1978). Otherwise, significant errors will be introduced if the geoid is used to infer GPE when dynamic topography is present. Moreover, the geoid anomalies, and hence the computed GPE values, are also sensitive to the filtering techniques. Note that the integral in (16) is not equivalent to the vertical integral of vertical stress, σ_{zz}, or GPE, which is correctly shown in eq. (7). Instead,

$$\int_0^L \rho(z) g z \, \mathrm{d}z = \bar{\sigma}_{zz} - \int_{-h}^0 \rho(z) z g \, \mathrm{d}z + L\int_{-h}^L \rho(z) g \, \mathrm{d}z. \tag{17}$$

Hence, the geoid can only be used as a proxy for GPE if the right most integral in (17) is a constant at reference depth L, meaning there is no dynamic topography (Flesch *et al.* 2007). Note that if the last term in (17), the pressure at reference depth L, varies over long wavelengths, then the geoid can be used as a proxy for GPE over length scales where those lateral variations in pressure are small. For example, for regional scale models such as North America, it may be appropriate to use the geoid as a proxy for GPE (Humphreys & Coblentz 2007).

For comparison purposes, we evaluate the deviatoric stress field associated with GPE inferred from the geoid to quantify the differences from a solution directly inferred from crustal structure. We use the EGM96 geoid model to approximate the GPE, with reference to a mid-oceanic ridge column of lithosphere (after Coblentz *et al.* 1994). Like Flesch *et al.* (2001), and Jones *et al.* (1996) before them, we filter the geoid such that terms below degree and order 7 are removed with a cosine taper to degree and order 11. A constant crustal and mantle density of 2828 and 3300 kg m^{-3} are assumed (after Flesch *et al.* 2001). The deviatoric stresses are computed in the same way as from the Crust 2.0 model.

There are many differences between the deviatoric stresses calculated from the geoid data set and those from the Crust 2.0 model. Both GPE differences and the deviatoric stress field (Fig. 7) are in general lower than those from the Crust 2.0 solutions. The deviatoric tension in western North America does not show up in the geoid solution. For the geoid solution, deviatoric compression in Northern Europe, the Southeast Asian subduction zone and the North American continent change to deviatoric tension, or strike-slip style of deformation. The mid-oceanic ridges in the geoid case constitute a much weaker signal than in the Crust 2.0 solutions. The matching of deviatoric stresses for the Indo-Australian plate with the SH_{max} directions of the WSM is considerably poorer for the geoid case. Similar differences exist between the geoid and uncompensated solution (Fig. 2), with the differences in magnitudes being greater.

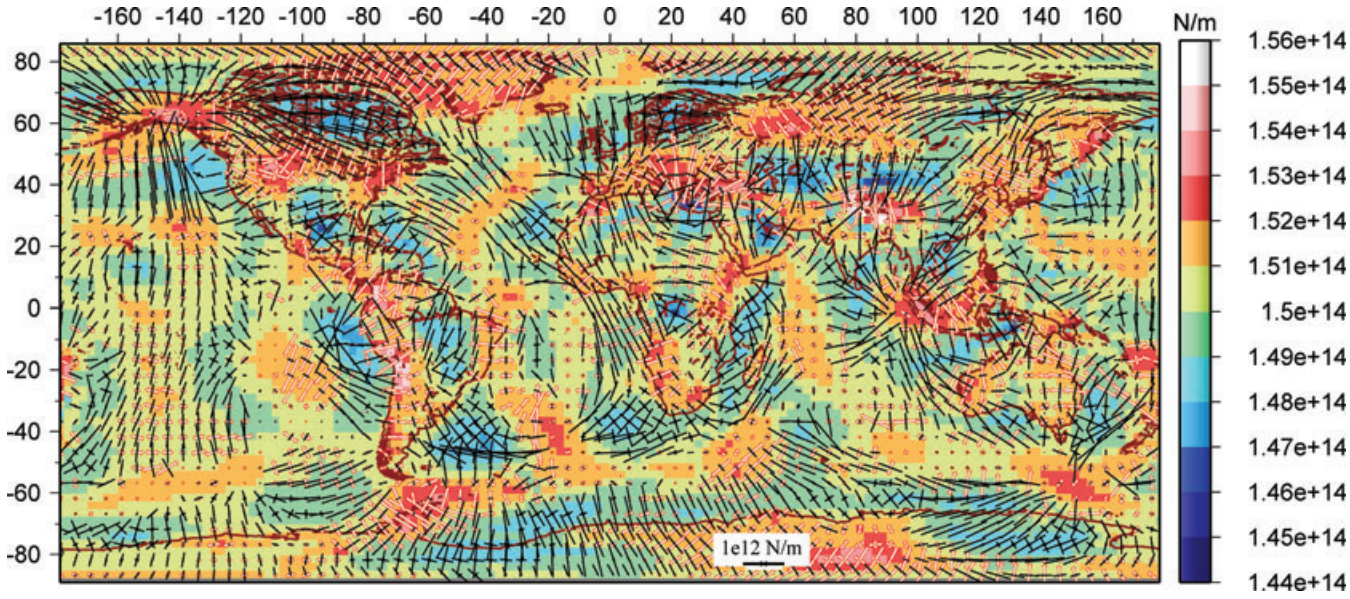

Figure 7. Global distribution of vertically integrated horizontal deviatoric stresses and GPE inferred from the EGM96 geoid data set.

7 REFERENCE LEVELS

For an uncompensated case, choice of reference level for the calculation of GPE has significant impact on the inferred deviatoric stresses associated with internal density buoyancy distributions in the lithosphere. Gravitational potential energy values must be computed with respect to some reference level and, depending on which reference level is chosen, the calculated GPE, and the associated deviatoric stresses, will change if the topography is uncompensated. Historically, there has been a precedence of calculating GPE with the surface of the geoid (sea level) as the reference level (Fleitout & Froidevoux 1982; Fleitout 1991; Coblentz *et al.* 1994; Jones *et al.* 1996; Zoback & Mooney 2003). Fleitout (1991) gave the 'moment law':

$$\int_0^L \Delta\sigma_{zz}(z)\,\mathrm{d}z = \delta mgd, \tag{18}$$

which states that the influence of an intralithospheric mass anomaly is proportional to its moment, the product of its amplitude δmg and depth d. This means that the greater the depth of the mass anomaly, the larger the impact on the GPE and the associated stress field. If the sea surface is treated as reference level, the above relation can be re-written as

$$\int_0^L \Delta\sigma_{zz}(z)\mathrm{d}z = g\int_0^L \Delta\rho(z)z\,\mathrm{d}z. \tag{19}$$

On the other hand, if we consider a constant depth level of L that is the maximum depth of integration, as the reference level, then the moment equation will be modified to

$$\int_0^L \Delta\sigma_{zz}(z)\,\mathrm{d}z = \int_0^L \left[\int_0^z \Delta\rho(z')g\,\mathrm{d}z'\right]\mathrm{d}z = \int_0^L (L-z)\Delta\rho(z)g\,\mathrm{d}z = \delta mg(L-z). \tag{20}$$

This implies that the near-surface density anomalies will have a greater effect on GPE, and the corresponding deviatoric stress field, than deeper anomalies within the portion of the lithosphere considered in the depth integrals. However, the differences in reference level are only relevant when topography is uncompensated. In the compensated case, the term in (20), $\sigma_{zz}(L)$, is a constant and the remaining term, $\int_0^L z\Delta\rho(z)g\mathrm{d}z$ is identical to that in (19), where the reference level is sea level. Although the inferred value of GPE is different, depending on whether (18) or (20) is used, because deviatoric stress depends only on the gradient in GPE, (18) and (20) yield the same result when $\sigma_{zz}(L)$ is a constant. However, when vertical stress $\sigma_{zz}(L)$ varies at the reference level, L, however, use of (18) and (20) will yield different estimates of deviatoric stress. Recall that the thin sheet equations arise from depth integration of the full 3-D force balance equations, with limits of integration from the surface, down to the reference level, L. The GPE term thus arises from the depth integration of the vertical stress, $\bar{\sigma}_{zz}$. To remain consistent with the thin sheet approach, the only appropriate form for GPE is therefore equation (20), where the reference level is at depth L.

8 DEVIATORIC STRESS MAGNITUDES

We argue that many previous calculations of depth integrals or depth averages of deviatoric stress magnitudes in Tibet as well as in the mid-oceanic ridges, have been overestimated (Ghosh *et al.* 2006). Maximum difference in depth integrals of deviatoric stress between Tibet and surrounding lowlands ($\bar{\tau}_{xx}|_{Tibet} - \bar{\tau}_{xx}|_{lowlands}$) is around 3.5–4 $\times 10^{12}$ N m^{-1}, which is about a factor of two lower than previous estimates of deviatoric stress difference ($\sim$6–7 $\times 10^{12}$ N m^{-1}) there (Molnar & Lyon-Caen 1988; Molnar *et al.* 1993). Also, the ridge-push force, or the vertically integrated deviatoric stress magnitudes associated with the mid-oceanic ridges in our solution ($\sim$1.5 $\times 10^{12}$ N m^{-1}), is lower than previous estimates of ridge-push ($\sim$3 $\times 10^{12}$ N m^{-1}) (Harper 1975; Lister 1975; Parsons & Richter 1980). This difference in deviatoric stress magnitudes from previous estimates can be attributed to two factors: (i) either a 2-D approximation of the thin sheet applied along a single profile and/or (ii) the form assumed for the hydrostatic state of stress, or both (Dalmayrac & Molnar 1981; Molnar & Lyon-Caen 1988). We use the term hydrostatic stress to refer to the reference pressure, P, subtracted from the total stress to obtain the deviatoric stress: $\tau_{ij} = \sigma_{ij} - P\delta_{ij}$. If P is assumed to be the lithostatic or vertical stress, σ_{zz}, then the deviatoric stress is defined as $\tau_{ij} = \sigma_{ij} - \sigma_{zz}\,\delta_{ij}$ (which we call 2-D definition of deviatoric stress). Such an assumption implies that the vertical component of the deviatoric stress, $\bar{\tau}_{zz}$, is equal to 0, which is entirely a special case, and is unlikely to be applicable in many areas (Engelder 1994). If P is defined as the mean stress, then deviatoric stress becomes $\tau_{ij} = \sigma_{ij} - \frac{1}{3}\sigma_{kk}\delta_{ij}$ (which we call a 3-D definition of deviatoric stress), with the constraint $\bar{\tau}_{xx} + \bar{\tau}_{yy} + \bar{\tau}_{zz} = 0$ (Flesch *et al.* 2001).

The largest estimates of deviatoric stresses have resulted from solutions to simplified 2-D thin sheet equations, applied along a single profile, along with the assumption that hydrostatic stress P is equal to the vertical stress, and $\tau_{zz} = 0$. In that case, the two horizontal force balance equations reduce to a single equation:

$$\frac{\partial\sigma_{xx}}{\partial x} = 0, \tag{21}$$

which, after using a 2-D definition of deviatoric stress, gives $\bar{\tau}_{xx} = -\bar{\sigma}_{zz} +$ a constant C as a solution to the depth integrated force balance equation. That is, the depth integrated deviatoric stress magnitude equals GPE. On the other hand, using the same force balance equation, but a definition of hydrostatic stress as the mean stress, yields $\bar{\tau}_{xx} = -\frac{1}{2}\bar{\sigma}_{zz} +$ a constant C, a magnitude of a factor of two lower than the previous case. The reason for lower stresses using the 3-D definition of deviatoric stress is that some of the potential energy differences get absorbed in the vertical term $\bar{\tau}_{zz}$, which is zero in the case with the 2-D definition.

Using the 3-D force balance equations, one of the horizontal deviatoric stresses, say $\bar{\tau}_{xx}$, can be given as

$$\bar{\tau}_{xx}^{3D} = \sigma_{xx} - \frac{1}{3}(\sigma_{xx} + \sigma_{yy} + \sigma_{zz}) \tag{22}$$

and

$$\bar{\tau}_{xx}^{2D} = \sigma_{xx} - \sigma_{zz}, \tag{23}$$

according to the 3-D and the 2-D definitions of deviatoric stress, respectively. From this, the relation between the 2-D and the 3-D deviatoric stresses can be written as

$$\bar{\tau}_{xx}^{2D} = 2\bar{\tau}_{xx}^{3D} + \bar{\tau}_{yy}^{3D}, \tag{24}$$

and similarly,

$$\bar{\tau}_{yy}^{2D} = 2\bar{\tau}_{yy}^{3D} + \bar{\tau}_{xx}^{3D} \tag{25}$$

$$\bar{\tau}_{xy}^{2D} = \bar{\tau}_{xy}^{3D}. \tag{26}$$

The reason for still lower stresses by using the full 3-D equations is the presence of the horizontal terms $\bar{\tau}_{yy}$ and $\bar{\tau}_{xy}$ which are absent in the case represented by a profile (eq. 21). Solutions using the full 3-D force balance equations, but a 2-D definition of deviatoric stress, yield deviatoric stress magnitudes a factor of two or more higher than our previous 3-D solutions (Fig. 8).

One importance of evaluating the correct magnitude of deviatoric stresses lies in the fact that the onset of deformation of the Indian ocean lithosphere has been explained by the high deviatoric stress magnitude ($\sim 8 \times 10^{12}$ N m^{-1}) in that area associated with the large GPE differences between Tibet and the Indian Ocean (Molnar *et al.* 1993). According to Molnar *et al.* (1993), a sediment laden oceanic lithosphere would be capable of buckling at a deviatoric stress magnitude of $\sim 4.4 \times 10^{12}$ N m^{-1}. We do not disagree with this. However, the vertically integrated deviatoric stress magnitude in that area, associated with the large GPE differences between Tibet and surrounding Indian Ocean, is not more than ~ 1.5–3×10^{12} N m^{-1} (Fig. 2, C1d). Therefore, deviatoric stresses required to produce the buckling must arise from additional sources other than GPE differences alone. Moreover, the magnitude of the ridge-push force has been used to constrain the intra-plate stress magnitude of the Indo-Australian plate (Reynolds *et al.* 2002) and to infer the degree of slab-plate coupling for the Java and Sumatra slabs (Sandiford *et al.* 2005). However, GPE differences between ridge and surrounding regions is insufficient to cancel the N–S deviatoric tension in Tibet associated with the excess GPE of Tibet (Figs 2–4 and C1a) (Ghosh *et al.* 2006). Because the total depth integrated deviatoric stress acting on the lithosphere can be attributed to stress related to (1) GPE differences and (2) horizontal basal tractions arising from deeper density buoyancies, the insufficiency of the ridge-push force in balancing the deviatoric tension at the Tibetan plateau calls for additional deviatoric stresses of magnitude ~ 2–3×10^{12} N m^{-1} associated with driving shear tractions at the base of the lithosphere in the Indian plate region (Ghosh *et al.* 2008). The density buoyancy distribution giving rise to these driving tractions is related to the long history of subduction of the Indian and Australian plates (Lithgow-Bertelloni & Richards 1995; Wen & Anderson 1997).

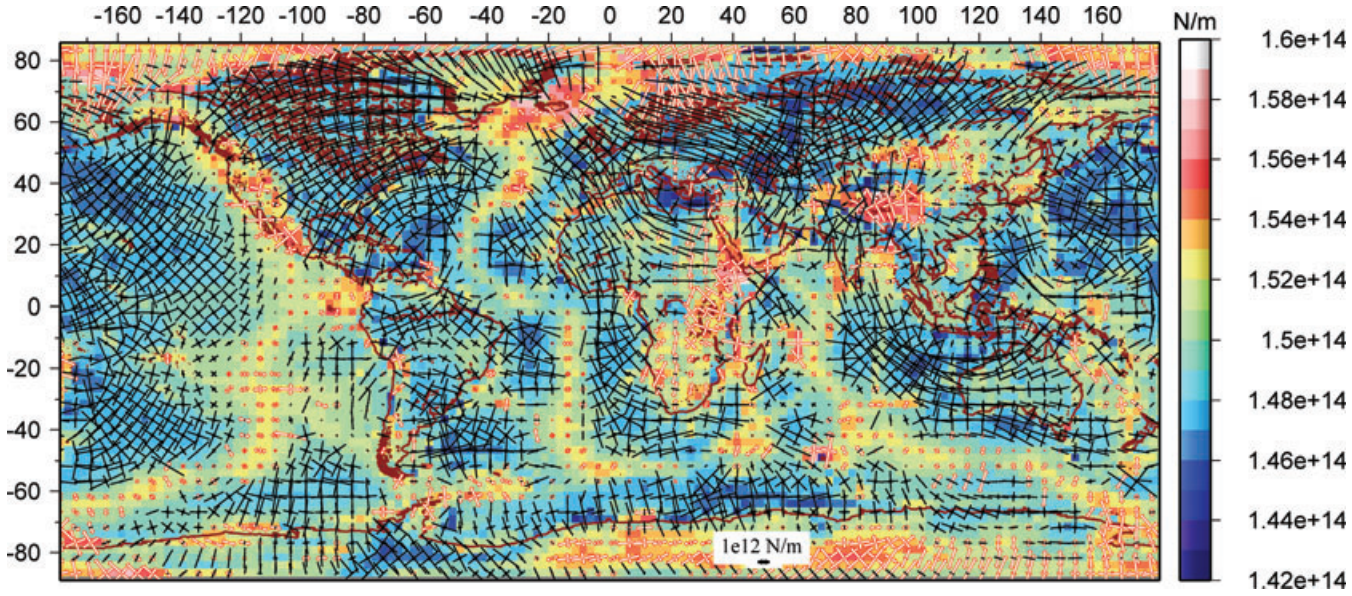

Figure 8. Global distribution of vertically integrated horizontal deviatoric stresses, calculated from an uncompensated Crust 2.0 model, based on a 2-D definition of deviatoric stress (eqs 24–26). The stress magnitudes are a factor of two higher than all our previous solutions, calculated using a 3-D definition.

9 COMPARISON OF CALCULATED DEVIATORIC STRESSES WITH THE STRAIN RATE TENSOR FIELD IN THE PLATE BOUNDARY ZONES

We introduce a quantitative way of testing our modelled deviatoric stresses with strain rate information from the Global Strain Rate Map (Kreemer *et al.* 2003; Holt *et al.* 2005). The Global Strain Rate Map (GSRM) is a velocity gradient tensor field solution for the entire Earth's surface. It is a high-resolution data set along the Earth's diffuse plate boundary zones. The GSRM model is based on 5170 GPS stations as well as Quarternary fault slip rate data. Our calculated deviatoric stress tensor is scored with the strain rate tensor from GSRM and we seek to match direction of principal axes as well as style of faulting. We define a correlation coefficient (Flesch *et al.* 2007)

$$-1 \leq \sum_{areas}(\epsilon \cdot \tau)\Delta S / \left(\sqrt{\sum_{areas}(E^2)\Delta S} * \sqrt{\sum_{areas}(T^2)\Delta S}\right) \leq 1 \tag{27}$$

where

$$E = \sqrt{\epsilon_{xx}^2 + \epsilon_{yy}^2 + \epsilon_{zz}^2 + \epsilon_{xy}^2 + \epsilon_{yx}^2} = \sqrt{2\epsilon_{xx}^2 + 2\epsilon_{xx}\epsilon_{yy} + 2\epsilon_{yy}^2 + 2\epsilon_{xy}^2},$$

$$T = \sqrt{\tau_{xx}^2 + \tau_{yy}^2 + \tau_{zz}^2 + \tau_{xy}^2 + \tau_{yx}^2} = \sqrt{2\tau_{xx}^2 + 2\tau_{xx}\tau_{yy} + 2\tau_{yy}^2 + 2\tau_{xy}^2}$$

and

$$\epsilon \cdot \tau = 2\epsilon_{xx}\tau_{xx} + \epsilon_{xx}\tau_{yy} + \epsilon_{yy}\tau_{xx} + 2\epsilon_{yy}\tau_{yy} + 2\epsilon_{xy}\tau_{xy}.$$

E and T are the second invariants of strain rate and deviatoric stress, respectively, ϵ_{ij} are strain rates from Kreemer *et al.* (2003), ΔS is the grid area and τ_{ij} are the calculated vertically integrated deviatoric stresses. Normalization of $\epsilon \cdot \tau$ by E and T in eq. (27) ensures that the correlation coefficient has no dependence on stress or strain rate magnitudes. The correlation coefficient only depends on a match of the deviatoric stress tensor to the inferred style of faulting (relative magnitude of extensional and compressional strain rate principal axes) and the match to the directions of principal axes between the stress and the strain rate tensors. A maximum correlation coefficient of $+1$ indicates perfect fit. That is, the stress tensor and the strain rate tensor are exactly the same in terms of style and direction of principal axes, whereas a coefficient of -1 indicates anti-correlation. For example, if the observed strain rate shows thrust faulting in an area, whereas our calculated deviatoric stress predicts normal faulting in the same area, then the correlation coefficient will predict a value of -1. A value of 0 will imply that the stress and the strain are uncorrelated. That is, for example, our modelled stresses predicting strike-slip faulting in an area of thrust or normal faulting, where the compressional and extensional principal axes differ from those in the GSRM by 45°.

The stress predictions from the different crustal and geoid models (Crust 2.0 and EGM96 Geoid) are compared with the strain rate tensor field from GSRM. Such a comparison provides a quantitative means of evaluating the contribution that the GPE differences make to the total stress tensor field within the plate boundary zones. A poor match, for example, highlights regions where additional stress component associated with deeper density buoyancies, and associated tractions, are necessary to explain the deformation indicators, and hence total deviatoric stress field. Higher correlation coefficients indicate a closer match between the stress tensor and strain tensor fields. Amongst the different models that we test, the best fit to the deformation indicators is given by the one calculated from Crust 2.0 model, compensated by density adjustment at 100 km, and with viscosities dependent only on strain rates (with reference viscosity ∼1/30, Fig. 3). The overall correlation for this model is 0.60 (Table 1). Nevertheless, individual regions react differently to different models. For example, for a 100 km reference level, the uncompensated model provides the best fit in areas like Eastern Africa and the Mediterranean (Tables 1 and 2, Figs 9 and C2c,e), whereas in regions such as the Andes, Central Asia and to some extent the Western Pacific, the Indo-Australian plate boundary zone

Table 1. Correlation coefficients obtained from a comparison between different deviatoric stress models with the strain rate tensor field from the GSRM model (see eq. 27) with reference level, $L = 100$ km and viscosities varying as a function of strain rates only (Fig. 1a).

Region of	Number	$\mu_{\text{ref}} \sim \frac{1}{3}$			$\mu_{\text{ref}} \sim \frac{1}{30}$			$\mu_{\text{ref}} \sim \frac{1}{300}$			$\mu_{\text{ref}} \sim \frac{1}{3000}$		
interest	of areas	U	CD	CE	U	CD	CE	U	CD	CE	U	CD	CE
Western North America	132	0.39	0.66	0.74	0.53	0.72	0.75	0.44	0.68	0.75	0.45	0.70	0.73
Andes	89	0.14	0.60	−0.04	0.25	0.69	0.06	0.15	0.54	−0.04	0.22	0.67	0
Eastern Africa	164	0.40	0.09	0.10	0.31	−0.04	−0.06	0.38	0.16	0.06	0.40	−0.01	0.04
Mediterranean	83	0.52	0.44	0.49	0.55	0.52	0.50	0.55	0.54	0.49	0.50	0.48	0.46
Central Asia	187	0.26	0.33	0.14	0.32	0.41	0.32	0.31	0.42	0.30	0.30	0.38	0.27
Indo-Australian plate boundary	174	0.68	0.71	0.70	0.69	0.77	0.74	0.64	0.61	0.67	0.60	0.70	0.67
Mid-oceanic ridges	292	0.82	0.86	0.87	0.79	0.85	0.87	0.77	0.83	0.84	0.66	0.76	0.76
Western Pacific	109	0.48	0.62	0.56	0.51	0.60	0.53	0.42	0.58	0.42	0.46	0.57	0.52
Southeast Asia	167	0.48	0.62	0.59	0.61	0.68	0.65	0.54	0.66	0.58	0.55	0.65	0.61
Total	1944	0.51	0.57	0.51	0.54	0.60	0.52	0.50	0.58	0.49	0.50	0.56	0.49

Note: The abbreviations U, CD and CE denote models that are uncompensated, compensated by density adjustment and compensated by elevation adjustment, respectively.

Table 2. Same as Table 1 but with viscosities varying as a function of both strain rates and lithosphere thickness (Fig. 1b).

Region of	Number	$\mu_{ref} \sim \frac{1}{3}$			$\mu_{ref} \sim \frac{1}{30}$			$\mu_{ref} \sim \frac{1}{300}$			$\mu_{ref} \sim \frac{1}{3000}$		
interest	of areas	U	CD	CE	U	CD	CE	U	CD	CE	U	CD	CE
Western North America	132	0.47	0.65	0.71	0.56	0.69	0.72	0.52	0.69	0.75	0.44	0.66	0.68
Andes	89	0.48	0.83	0.36	0.51	0.86	0.37	0.44	0.84	0.24	0.41	0.83	0.23
Eastern Africa	164	0.20	−0.31	−0.27	0.08	−0.35	−0.32	0.24	−0.17	−0.17	0.30	−0.3	−0.18
Mediterranean	83	0.44	0.40	0.44	0.52	0.48	0.51	0.55	0.52	0.49	0.50	0.43	0.49
Central Asia	187	0.25	0.33	0.20	0.33	0.40	0.36	0.37	0.46	0.39	0.29	0.37	0.33
Indo-Australian plate boundary zone	174	0.65	0.75	0.70	0.60	0.75	0.68	0.61	0.72	0.69	0.56	0.68	0.62
Mid-oceanic ridges	292	0.70	0.81	0.81	0.63	0.78	0.78	0.65	0.76	0.76	0.53	0.64	0.65
Western Pacific	109	0.56	0.63	0.61	0.58	0.60	0.59	0.57	0.61	0.57	0.53	0.58	0.57
Southeast Asia	167	0.57	0.61	0.61	0.66	0.68	0.68	0.63	0.68	0.66	0.61	0.66	0.64
Total	1944	0.50	0.53	0.49	0.50	0.54	0.50	0.52	0.57	0.51	0.48	0.51	0.47

and Southeast Asia, the best fit is given by a model compensated by density adjustment (Tables 1 and 2). A model compensated by adjusting the topography, on the other hand, gives the best fit to the strain rate tensor data in western North America, as well as in the mid-oceanic ridges (Tables 1 and 2). In general, areas of continental deformation such as Central Asia (Fig. C2a), western North America (Fig. C2b) and the Andes (Fig. 9), including areas such as to the Southeast of Africa (Fig. C2e) yield a poor fit to the deformation indicators. The Central Indian Ocean (Fig. C2d), on the other hand, shows a very good match.

Models with viscosities varying as a function of both strain rates and lithosphere thickness fare worse when the overall fit is considered (Table 2), with a highest correlation coefficient of 0.57 (with reference viscosity ∼1/300). The overall poor fit could potentially arise from errors in the lithosphere thickness model. However, some areas, such as the Andes, and to a certain extent Central Asia, Southeast Asia, and the Western Pacific, exhibit an improved fit when viscosities along plate boundaries are allowed to vary with lithospheric thickness as well. A lithospheric model with a laterally uniform viscosity structure provides a poor fit to the strain rate tensor data (Table 3) with an overall correlation coefficient of 0.31.

For models inclusive of deeper density buoyancy within the keels, the only region that undergoes some improvement in fitting is Africa (Tables 4 and 5, Fig. 6). For all the other areas the fit either degrades or stays unchanged.

The Geoid model displays a poor fit in almost all the areas (Tables 6 and 7) with the exception of the mid-oceanic ridges. However, the fit to the mid-oceanic ridges is still worse than in the Crust 2.0 case. In fact, the mid-oceanic ridges show high correlation for both the Crust 2.0 and the EGM96 models. The failure of the Geoid model to match the observed deformation in the plate boundaries could be associated with the sensitivity of the geoid anomalies, and consequently the GPE values, to the filtering techniques. Calculation of GPE from geoid anomalies also assumes no dynamic topography, as mentioned earlier in Section 6. The assumptions embedded in the use of geoid as a proxy for GPE

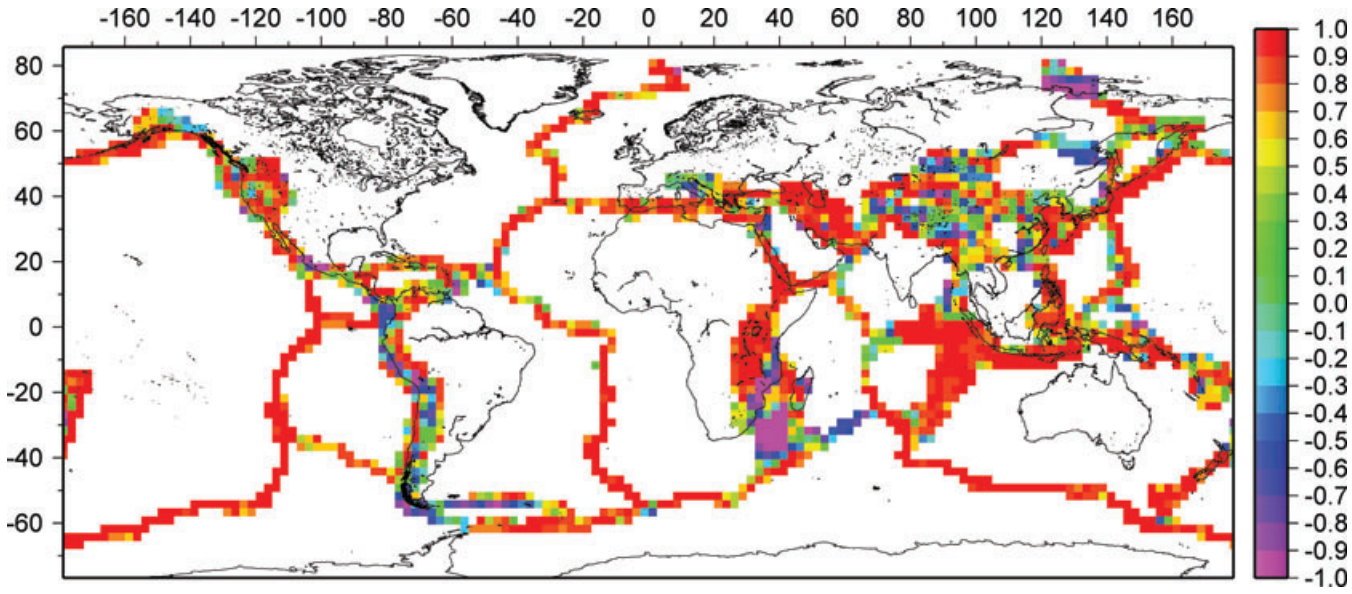

Figure 9. Correlation coefficients between observed strain rate tensors from the GSRM and deviatoric stress tensors, varying as a function of strain rates only, arising from GPE differences from an uncompensated Crust 2.0 model (Fig. 2).

Table 3. Correlation coefficients obtained from comparison between deviatoric stress field from an uncompensated Crust 2.0 model with the strain rate tensor field from the GSRM model with laterally uniform viscosity in the lithosphere.

Region of interest	Number of areas	$\mu_{\rm ref} = 1$
Western North America	132	0.08
Andes	89	−0.20
Eastern Africa	164	0.63
Mediterranean	83	0.33
Central Asia	187	0.10
Indo-Australian plate boundary zone	174	0.30
Mid-oceanic ridges	292	0.78
Western Pacific	109	0.09
Southeast Asia	167	0.08
Total	1944	0.31

Table 4. Correlation coefficients obtained from a comparison between different deviatoric stress models with the strain rate tensor field from the GSRM model with reference level $L = 270$ km and viscosities varying as a function of strain rates only.

Region of interest	Number of areas	$\mu_{\rm ref} \sim \frac{1}{3}$	$\mu_{\rm ref} \sim \frac{1}{30}$	$\mu_{\rm ref} \sim \frac{1}{300}$	$\mu_{\rm ref} \sim \frac{1}{3000}$
Western North America	132	0.44	0.57	0.50	0.50
Andes	89	0.21	0.35	0.22	0.30
Eastern Africa	164	0.45	0.40	0.45	0.43
Mediterranean	83	0.51	0.54	0.53	0.48
Central Asia	187	0.24	0.27	0.26	0.26
Indo-Australian plate boundary zone	174	0.74	0.77	0.72	0.73
Mid-oceanic ridges	292	0.86	0.84	0.82	0.73
Western Pacific	109	0.52	0.53	0.45	0.49
Southeast Asia	167	0.61	0.66	0.61	0.63
Total	1944	0.55	0.58	0.54	0.54

may therefore only be appropriate for regional scale modelling (e.g. Humphreys & Coblentz 2007), but on a global scale are problematic due to the importance of dynamic topography.

The low to moderate values of correlation coefficients in many areas imply the inadequacy of lateral density variations within the lithosphere alone to satisfy the observed deformation. Stresses, arising from density buoyancy-driven basal tractions are required to explain the observed deformation along the plate boundaries (Ghosh *et al.* 2008). Ghosh *et al.* (2008) have shown a universal improvement in fit for all regions when tractions associated with deeper density buoyancies are included. The role and need for such tractions is especially marked in areas of high GPE, such as Central Asia (Figs 9 and C2a), where nearly pure tension is predicted by the GPE differences, but deformation yields dominant strike-slip faulting there. The tractions associated with deeper mantle buoyancies integrate over great distances and provide, for example, the needed compressional deviatoric stresses, which act together with GPE differences to provide total deviatoric stresses across Tibet and the Andes in accord with deformation indicators (Ghosh *et al.* 2008).

10 CONCLUSIONS

The two main factors controlling lithospheric stress field are (1) gravitational potential energy differences arising from GPE variations within the lithosphere and (2) horizontal basal tractions arising from mantle convection, which are coupled to the base of the lithosphere. In this study, we quantify only the first of the above two factors. We show that dynamic topography likely makes a significant contribution to GPE differences and the deviatoric stresses associated with these GPE differences (compare Figs 2 and 4). A correct quantification of (1) will enable us to estimate the bounds on (2), the magnitude of the horizontal basal tractions associated with lithospheric coupling with deeper mantle circulation. If dynamic topography can be removed from the GPE model (e.g. Fig. 4), then it is possible to infer the relative contribution of GPE differences arising from lithospheric buoyancies alone and the contributions arising from deeper mantle circulation involving both radial and horizontal tractions.

We calculate GPE from the Crust 2.0 and the EGM96 geoid models using both uniform lithospheric viscosity and varying viscosities for plate boundaries as well as intraplate regions and show that laterally varying lithospheric strength is required to match the observed stress and strain rate pattern. We take into account deeper density buoyancies associated with cratonic roots. We find that inclusion of deeper lithospheric density buoyancies has little effect on the style and direction of the deviatoric stress field. Moreover, consideration of these deeper density buoyancies in the keels is based on the premise that there is no buoyancy driven mantle convection and no dynamic topography. A simpler model excluding the deeper keels fits the deformation indicators better. We clarify the usage of a correct level of reference (maximum depth

Table 5. Same as Table 4, but with viscosities varying as a function of both strain rates and lithosphere thickness.

Region of interest	Number of areas	$\mu_{\rm ref} \sim \frac{1}{3}$	$\mu_{\rm ref} \sim \frac{1}{30}$	$\mu_{\rm ref} \sim \frac{1}{300}$	$\mu_{\rm ref} \sim \frac{1}{3000}$
Western North America	132	0.52	0.60	0.56	0.47
Andes	89	0.56	0.60	0.54	0.51
Eastern Africa	164	0.26	0.13	0.27	0.28
Mediterranean	83	0.43	0.50	0.51	0.48
Central Asia	187	0.24	0.29	0.32	0.25
Indo-Australian plate boundary zone	174	0.69	0.67	0.70	0.62
Mid-oceanic ridges	292	0.76	0.69	0.69	0.58
Western Pacific	109	0.57	0.58	0.56	0.54
Southeast Asia	167	0.61	0.69	0.68	0.65
Total	1944	0.53	0.54	0.55	0.50

Table 6. Correlation coefficients obtained from a comparison between different deviatoric stress models from the Geoid data set with the strain rate tensor field from the GSRM model with viscosities varying as a function of strain rates only.

Region of interest	Number of areas	$\mu_{\rm ref} \sim \frac{1}{3}$	$\mu_{\rm ref} \sim \frac{1}{30}$	$\mu_{\rm ref} \sim \frac{1}{300}$	$\mu_{\rm ref} \sim \frac{1}{3000}$
Western North America	132	−0.31	−0.20	−0.20	−0.22
Andes	89	−0.32	−0.31	−0.30	−0.34
Eastern Africa	164	−0.03	−0.06	−0.03	−0.04
Mediterranean	83	0.15	0.32	0.32	0.22
Central Asia	187	0.24	0.34	0.36	0.28
Indo-Australian plate boundary zone	174	0.29	0.46	0.41	0.35
Mid-oceanic ridges	292	0.81	0.81	0.76	0.62
Western Pacific	109	−0.06	−0.07	−0.09	−0.13
Southeast Asia	167	0.20	0.23	0.19	0.17
Total	1944	0.17	0.22	0.21	0.15

of integration) for a thin sheet approach and show that GPE and associated deviatoric stresses calculated from geoid do not fit the observed deformation in the Earth's deforming plate boundary zones. The poor fit may be related to filtering methods, but we emphasize that on a global scale, the geoid should be used with caution for inferring GPE. That is, the usage of the geoid to infer GPE involves the assumption that there is no dynamic topograpy signature in the Earth's gravity field. We also demonstrate how a 2-D definition of deviatoric stress, along with 2-D force balance equations, can yield overestimates of the depth integrals of the deviatoric stress magnitudes. Finally, we use a quantitative way of testing our stress models with strain rate information from Global Strain Rate Map. The stress models indicate that GPE differences are an important component of the total global stress field. However, GPE differences by themselves are, in general, insufficient to explain the total deviatoric stress field, particularly in areas such as Eastern Africa, Andes, and Central Asia; an added contribution from basal tractions is required to explain the observed discrepancies between the models and observations (Ghosh *et al.* 2008). Although these basal tractions are not in general large, they integrate over long distances to provide substantial additional stress input into the lithosphere (Bird *et al.* 2008; Steinberger *et al*. 2001; Lithgow *et al*. 2009; Ghosh *et al*. 2008).

ACKNOWLEDGMENTS

We would like to thank John Haines for helpful discussions and Lada Dimitrova for input regarding reference level. Reviews by Bernhard Steinberger and David Coblentz greatly improved the manuscript. Figures were prepared using GMT 3.4.4 and 4.3.1 by P. Wessel and W. F. Smith. This research was funded by NSF grants EAR-031019, EAR-0545606 and EAR-0538437.

REFERENCES

Airy, G.B., 1855. On the computation of the effect of the attraction of mountain-masses, as disturbing the apparent astronomical latitude of stations of geodetic surveys, *Roy. Soc. Lond. Phil. Trans.,* **145,** 101–104.

Artyushkov, E.V., 1973. Stresses in the lithosphere caused by crustal thickness inhomogeneities, *J. geophys. Res.,* **78,** 7675–7690.

Beavan, J. & Haines, J., 2001. Contemporary horizontal velocity and strain rate fields of the Pacific-Australian plate boundary zone through New Zealand, *J. geophys. Res.,* **106,** 741–770.

Becker, T.W. & O'Connell, R.J., 2001. Predicting plate velocities with mantle circulation models, *Geochem., Geophys., Geosyst.,* **2,** GC000171.

Bird, P., Liu, Z. & Rucker, W.K., 2008. Stresses that drive the plates from below: Definitions, computational path, model optimization, and error analysis, *J. geophys. Res.,* **113,** B11406, doi:10.1029/2007JB005460.

Cazenave, A., Souriau, A. & Dominh, K., 1989. Global coupling of Earth surface topography with hotspots, geoid and mantle heterogeneities, *Nature,* **340,** 54–57.

Coblentz, D.D. & Sandiford, M., 1994. Tectonic stresses in the African plate: constraints on the ambient lithospheric stress state, *Geology,* **22,** 831–834.

Table 7. Same as Table 6, but with viscosities varying as a function of both strain rates and lithosphere thickness.

Region of interest	Number of areas	$\mu_{\rm ref} \sim \frac{1}{3}$	$\mu_{\rm ref} \sim \frac{1}{30}$	$\mu_{\rm ref} \sim \frac{1}{300}$	$\mu_{\rm ref} \sim \frac{1}{3000}$
Western North America	132	−0.33	−0.20	−0.19	−0.20
Andes	89	−0.27	−0.24	−0.27	−0.32
Eastern Africa	164	−0.11	−0.19	−0.10	−0.09
Mediterranean	83	0.17	0.31	0.27	0.19
Central Asia	187	0.25	0.36	0.38	0.31
Indo-Australian plate boundary zone	174	0.26	0.47	0.45	0.36
Mid-oceanic ridges	292	0.74	0.69	0.68	0.50
Western Pacific	109	−0.01	0	−0.04	−0.10
Southeast Asia	167	0.27	0.29	0.24	0.19
Total	1944	0.17	0.22	0.21	0.15

Coblentz, D.D., Richardson, R.M. & Sandiford, M., 1994. On the gravitational potential energy of the Earth's lithosphere, *Tectonophys.,* **13,** 929–945.

Coblentz, D.D., Sandiford, M., Richardson, R.M., Zhou, S. & Hillis, R., 1995. The origins of the intraplate stress field in continental Australia, *Earth planet. Sci. Lett.,* **133,** 299–309.

Conrad, C.P. & Lithgow-Bertelloni, C., 2006. Influence of continental roots and asthenosphere on plate-mantle coupling, *Geophys. Res. Lett.,* **33,** L05312, doi:10.1029/2005GL025621.

Dalmayrac, B. & Molnar, P., 1981. Parallel thrust and normal faulting in Peru and constraints on the state of stress, *Earth planet. Sci. Lett.,* **55,** 473–481.

de Boor, C.D., 1978. *A Practical Guide to Splines,* Springer-Verlag, New York.

Engelder, T., 1994. Deviatoric stressitis: a virus infecting the Earth science community, *EOS, Trans. Am. geophys. Un.,* **75,** 211–212.

England, P.C. & Houseman, G.A., 1986. Finite strain calculations of continental deformation, Part 2. Comparison with the India–Eurasia collision zone, *J. geophys. Res.,* **91,** 3664–3676.

England, P.C. & Jackson, J., 1989. Active deformation of the continents, *Ann. Rev. Earth Planet. Sci.,* **17,** 197–226.

England, P.C. & McKenzie, D.P., 1982. A thin viscous sheet model for continental deformation, *Geophys. J. R. astr. Soc.,* **70,** 295–321.

England, P.C. & Molnar, P., 1997. Active deformation of Asia, from kinematics to dynamics, *Science,* **278,** 647–650.

Fleitout, L., 1991. The sources of lithospheric tectonic stresses, *Roy. Soc. London Phil. Trans.,* **337,** 73–81.

Fleitout, L. & Froidevoux, C., 1982. Tectonics and topography for a lithosphere containing density heterogeneities, *Tectonophysics,* **1,** 21–56.

Fleitout, L. & Froidevoux, C., 1983. Tectonic stresses in the lithosphere, *Tectonophysics,* **2,** 315–324.

Flesch, L.M., Holt, W.E., Haines, A.J. & Shen-Tu, B., 2000. Dynamics of the Pacific-North American plate boundary in the western United States, *Science,* **287,** 834–836.

Flesch, L.M., Haines, A.J. & Holt, W.E., 2001. Dynamics of the India–Eurasia collision zone, *J. geophys. Res.,* **106,** 16 435–16 460.

Flesch, L.M., Holt, W.E., Haines, A.J., Wen, L. & Shen-tu, B., 2007. The dynamics of western North America: Stress magnitudes and the relative role of gravitational potential energy, plate interaction at the boundary, and basal tractions, *Geophys. J. Int.,* **169,** 866–896.

Frank, F.C., 1972. Plate tectonics, the analogy with glacier flow, and isostasy, *Flow and Fracture of Rocks, Geophys. Monogr. Ser.,* Vol. 16, pp. 285–292, eds Heard, H.C. et al., AGU, Washington, DC.

Ghosh, A., Holt, W.E., Haines, A.J. & Flesch, L.M., 2006. Gravitational potential energy of the Tibetan Plateau and the forces driving the Indian plate, *Geology,* **34,** 321–324.

Ghosh, A., Holt, W.E., Wen, L., Haines, A.J. & Flesch, L.M., 2008. Joint modeling of lithosphere and mantle dynamics elucidating lithosphere-mantle coupling, *Geophys. Res. Lett.,* **35,** L16309, doi:10.1029/2008GL034365.

Hager, B.H., Clayton, R.W., Richards, M.A., Comer, R.P. & Dziewonski, A.M., 1985. Lower mantle heterogeneity, dynamic topography and the geoid, *Nature,* **313,** 541–545.

Harper, J.F., 1975. On the driving forces of plate tectonics, *Geophys. J. R. astr. Soc.,* **40,** 465–474.

Haxby, W.F. & Turcotte, D.L., 1978. On isostatic geoid anomalies, *J. geophys. Res.,* **83,** 5473–5478.

Holt, W.E. & Haines, A., 1995. The kinematics of northern South Island, New Zealand, determined from geologic strain rates, *J. geophys. Res.,* **100,** 17 991–18 010.

Holt, W.E., Chamot-Rooke, N., Pichon, X.L., Haines, A., Shen-Tu, B. & Ren, J., 2000. Velocity field in Asia inferred from Quaternary fault slip rates and Global Positioning System observations, *J. geophys. Res.,* **105,** 19 185–19 209.

Holt, W.E., Kreemer, C., Haines, A., Estey, L., Meertens, C., Blewitt, G. & Lavallee, D., 2005. Project helps constrain continental dynamics and seismic hazards, *EOS, Trans. Am. geophys. Un.,* **86,** 383–387.

Houseman, G. & England, P., 1986. A dynamical model of lithosphere extension and sedimentary basin formation, *J. geophys. Res.,* **91,** 719–729.

Humphreys, E. & Coblentz, D., 2007. North American dynamics and western U.S. tectonics, *Rev. Geophys.,* **45,** RG3001, doi:10.1029/2005RG000181.

Iaffaldano, G., Bunge, H.P. & Dixon, T.H., 2006. Feedback between mountain belt growth and plate convergence, *Geology,* **34,** 893–896.

Jones, C.H., Unruh, J. & Sonder, L., 1996. The role of gravitational potential energy in active deformation in the southwestern United States, *Nature,* **381,** 37–41.

Klein, E.C., Flesch, L.M., Holt, W.E. & Haines, A.J., 2009. Evidence of long-term weakness on seismogenic faults in western North America from dynamic modeling, *J. geophys. Res.,* **114,** B03402, doi:10.1029/2007JB005201.

Kreemer, C., Holt, W.E. & Haines, A.J., 2003. An integrated global model of present-day plate motions and plate boundary deformation, *Geophys. J. Int.,* **154,** 8–34.

Lister, C.R.B., 1975. Gravitational drive on oceanic plates caused by thermal contraction, *Nature,* **257,** 663–665.

Lithgow-Bertelloni, C. & Guynn, J.H., 2004. Origin of the lithospheric stress field, *J. geophys. Res.,* **109,** B01408, doi:10.1029/2003JB002467.

Lithgow-Bertelloni, C. & Richards, M., 1995. Cenozoic plate driving forces, *Geophys. Res. Lett.,* **22,** 1317–1320.

Lithgow-Bertelloni, C. & Silver, P.G., 1998. Dynamic topography, plate driving forces and the African Superswell, *Nature,* **395,** 269–272.

McKenzie, D., 1972. Active tectonics of Mediterranean region, *Geophys. J. R. astr. Soc.,* **30,** 109–185.

Meade, B., 2007. Present-day kinematics at the India-Asia collision zone, *Geology,* **35,** doi:10.1130/G22942A.1.

Molnar, P., 1988. Continental tectonics in the aftermath of plate tectonics, *Nature,* **335,** 131–137.

Molnar, P. & Lyon-Caen, H., 1988. Some physical aspects of the support, structure, and evolution of mountain, *Spec. Paper Geol. Soc. Am.,* **218,** 179–207.

Molnar, P. & Tapponnier, P., 1975. Cenozoic tectonics of Asia: effects of a continental collision, *Science,* **189,** 419–425.

Molnar, P., England, P. & Martinod, J., 1993. Mantle dynamics, uplift of the Tibetan plateau, and the Indian monsoon, *Rev. Geophys.,* **31,** 357–396.

Morse, P.M. & Feshbach, H., 1953. *Methods of Theoretical Physics,* pp. 257–347, McGraw-Hill, New York.

Müller, R.D., Roest, W., Royer, J., Gahagan, L. & Sclater, J., 1997. Digital isochrons of the world's ocean floor, *J. geophys. Res.,* **102,** 3211–3214.

Panasyuk, S.V. & Hager, B.H., 2000. Models of isostatic and dynamic topography, geoid anomalies, and their uncertainties, *J. geophys. Res.,* **105,** 28 199–28 209.

Parsons, B. & Richter, F., 1980. A relation between the driving force and geoid anomaly associated with mid-oceanic ridges, *Earth planet. Sci. Lett.,* **51,** 445–450.

Pratt, J.H., 1855. On the attraction of the Himalaya mountains, and the elevated regions beyond them, upon the plumb line in India, *Phil. Trans. R. Soc. Lond., A* **145,** 55–100.

Reinecker, J., Heidbach, O., Tingay, M., Sperner, B. & Müller, B., 2005. The release 2005 of the World Stress Map, available at http://www.world-stress-map.org.

Reynolds, S.D., Coblentz, D. & Hillis, R., 2002. Tectonic forces controlling the regional intraplate stress field in continental Australia: results from new finite-element modelling, *J. geophys. Res.,* **107,** doi:10.1029/2001JB000408.

Sandiford, M. & Coblentz, D., 1994. Plate-scale potential-energy distributions and the fragmentation of ageing plates, *Earth planet. Sci. Lett.,* **126,** 143–159.

Sandiford, M., Coblentz, D. & Richardson, R., 1995. Ridge torques and continental collision in the Indian-Australian plate, *Geology,* **23,** 653–656.

Sandiford, M., Coblentz, D. & Schellart, W., 2005. Evaluating slab-plate coupling in the Indo-Australian plate, *Geology,* **33,** 113–116.

Stein, C.A. & Stein, S., 1992. A model for the global variation in oceanic depth and heat flow with lithospheric age, *Nature,* **1992,** 123–129.

Steinberger, B., 2007. Effect of latent heat release at phase boundaries on flow in the earth's mantle, phase boundary topography and dynamic topography at the earth's surface, *Phys. Earth planet. Int.,* **164,** doi:10.1016/j.pepi.2007.04.021.

Steinberger, B., Schmeling, H. & Marquart, G., 2001. Large-scale lithospheric stress field and topography induced by global mantle circulation, *Earth planet. Sci. Lett.,* **2001,** 75–91.

Thatcher, W., 2007. Microplate model for the present-day deformation of Tibet, *J. geophys. Res.,* **112,** 401, doi:10.1029/2005JB004244.

Turcotte, D. & Schubert, G., 1982. *Geodynamics: Applications of Continuum Physics to Geological Problems,* p. 450, John Wiley, New York.

Wen, L. & Anderson, D.L., 1997. Present-day plate motion constraint on mantle rheology and convection, *J. geophys. Res.,* **102,** 24 639–24 653.

Zoback, M.L., 1992. First and second order patterns of stress in the lithosphere: the World Stress Map Project, *J. geophys. Res.,* **102,** 11 703–11 728.

Zoback, M.L. & Mooney, W.D., 2003. Lithospheric buoyancy and continental intraplate stresses, *Int. Geol. Rev.,* **45,** 95–118.

APPENDIX A: SPHERICAL TREATMENT

In spherical coordinates, the x, y and z directions of cartesian coordinates change to the ϕ, θ and r (radial) components, respectively. The deviatoric stress tensor in the radial direction is

$$\tau_{rr} = \sigma_{rr} - \frac{1}{3}\sigma_{kk}, \tag{A1}$$

where σ_{rr} is the total stress tensor in the radial direction and $\frac{1}{3}\sigma_{kk}$ is the mean total stress. The total stress tensor, $\sigma_{ij} = \tau_{ij} + \frac{1}{3}\sigma_{kk}\delta_{ij}$, then becomes

$$\sigma_{ij} = \tau_{ij} + \delta_{ij}(\sigma_{rr} - \tau_{rr}), \tag{A2}$$

where δ_{ij} represents the Kronecker delta. The force balance eq. (1) can be written in spherical coordinates as

$$\frac{1}{\cos\theta}\frac{\partial}{\partial\phi}\left(r^2\sigma_{\phi\phi}\right) + \frac{1}{\cos^2\theta}\frac{\partial}{\partial\theta}\left(r^2\sigma_{\phi\theta}\cos^2\theta\right) + \frac{\partial}{\partial r}\left(r^3\sigma_{\phi r}\right) = 0 \tag{A3}$$

$$\frac{1}{\cos\theta}\frac{\partial}{\partial\phi}\left(r^2\sigma_{\phi\theta}\right) + \frac{1}{2}\frac{\partial}{\partial\theta}\left(r^2[\sigma_{\theta\theta} + \sigma_{\phi\phi}]\right) + \frac{1}{2\cos^2\theta}\frac{\partial}{\partial\theta}\left(r^2\cos^2\theta[\sigma_{\theta\theta} - \sigma_{\phi\phi}]\right) + \frac{\partial}{\partial r}\left(r^3\sigma_{\theta r}\right) = 0 \tag{A4}$$

$$\frac{1}{r\cos\theta}\frac{\partial\sigma_{\phi r}}{\partial\phi} + \frac{1}{r\cos\theta}\frac{\partial}{\partial\theta}(\cos\theta\sigma_{\theta r}) + \frac{1}{r}(2\sigma_{rr} - \sigma_{\phi\phi} - \sigma_{\theta\theta}) + \frac{\partial\sigma_{rr}}{\partial r} - \rho g = 0. \tag{A5}$$

Vertically integrating (A3) and (A4) yields

$$\frac{1}{\cos\theta}\frac{\partial}{\partial\phi}\left(\int_{r_L}^{r_0} r^2\sigma_{\phi\phi}\mathrm{d}r\right) + \frac{1}{\cos^2\theta}\frac{\partial}{\partial\theta}\left(\int_{r_L}^{r_0} r^2\sigma_{\phi\theta}\mathrm{d}r\cos^2\theta\right) + r_0^3\sigma_{\phi r}|_{r_0} - r_L^3\sigma_{\phi r}|_{r_L} = 0 \tag{A6}$$

and

$$\frac{1}{\cos\theta}\frac{\partial}{\partial\phi}\left(\int_{r_L}^{r_0} r^2\sigma_{\phi\theta}\mathrm{d}r\right) + \frac{1}{2}\frac{\partial}{\partial\theta}\left(\int_{r_L}^{r_0} r^2[\sigma_{\theta\theta} + \sigma_{\phi\phi}]\mathrm{d}r\right) + \frac{1}{2\cos^2\theta}\frac{\partial}{\partial\theta}\left(\int_{r_L}^{r_0} r^2\cos^2\theta[\sigma_{\theta\theta} - \sigma_{\phi\phi}]\mathrm{d}r\right) + r_0^3\sigma_{\theta r}|_{r_0} - r_L^3\sigma_{\theta r}|_{r_L} = 0 \tag{A7}$$

where r_0 is the radius from the centre of the Earth to the surface and r_L is the radius from the centre to the base of the lithosphere. Substituting (A2) in (A6) and (A7), we arrive at

$$\frac{1}{\cos\theta}\frac{\partial}{\partial\phi}\left(\int_{r_L}^{r_0} r^2\tau_{\phi\phi}\mathrm{d}r\right) - \frac{1}{\cos\theta}\frac{\partial}{\partial\phi}\left(\int_{r_L}^{r_0} r^2\tau_{rr}\mathrm{d}r\right) + \frac{1}{\cos^2\theta}\frac{\partial}{\partial\theta}\left(\cos^2\theta\int_{r_L}^{r_0} r^2\tau_{\phi\theta}\mathrm{d}r\right) + \frac{1}{\cos\theta}\frac{\partial}{\partial\phi}\left(\int_{r_L}^{r_0} r^2\sigma_{rr}\mathrm{d}r\right) - r_L^3\tau_{\phi r}|_{r_L} = 0 \tag{A8}$$

and

$$\begin{aligned}&\frac{1}{\cos\theta}\frac{\partial}{\partial\phi}\left(\int_{r_L}^{r_0} r^2\tau_{\phi\theta}\mathrm{d}r\right) + \frac{1}{2}\frac{\partial}{\partial\theta}\left(\int_{r_L}^{r_0} r^2\tau_{\theta\theta}\mathrm{d}r + \int_{r_L}^{r_0} r^2\tau_{\phi\phi}\mathrm{d}r\right) - \frac{\partial}{\partial\theta}\left(\int_{r_L}^{r_0} r^2\tau_{rr}\mathrm{d}r\right)\\ &+\frac{1}{2\cos^2\theta}\frac{\partial}{\partial\theta}\left(\cos^2\theta\left[\int_{r_L}^{r_0} r^2\tau_{\theta\theta}\mathrm{d}r - \int_{r_L}^{r_0} r^2\tau_{\phi\phi}\mathrm{d}r\right]\right) + \frac{\partial}{\partial\theta}\left(\int_{r_L}^{r_0} r^2\sigma_{rr}\mathrm{d}r\right) - r_L^3\tau_{\theta r}|_{r_L} = 0,\end{aligned} \tag{A9}$$

which are equivalent to eqs (5) and (6) in text. Note that $\sigma_{\phi r}|_{r_0}$ and $\sigma_{\theta r}|_{r_0}$ are zero. For a thin sheet, the gradients of $\sigma_{\phi r}$ and $\sigma_{\theta r}$ are negligibly small (see text). Moreover, the term $\frac{1}{r}(2\sigma_{rr} - \sigma_{\phi\phi} - \sigma_{\theta\theta})$ is small compared to ρg. Hence, (A5) can be approximated as

$$\frac{\partial \sigma_{rr}}{\partial r} - \rho g = 0 \tag{A10}$$

which implies

$$\sigma_{rr} = -\int_r^{r_0} \rho g \mathrm{d}r \tag{A11}$$

so that the GPE eq. (7) in spherical coordinates is equivalent to

$$\int_{r_L}^{r_0} r^2 \sigma_{rr} \mathrm{d}r = -\int_{r_L}^{r_0} r^2 \left[\int_r^{r_0} \rho g \mathrm{d}r'\right] \mathrm{d}r = -\int_{r_L}^{r_0} \rho g \left[\int_{r_L}^{r'} r^2 \mathrm{d}r\right] \mathrm{d}r' = -\int_{r_L}^{r_0} \frac{1}{3} \rho g \left(r'^3 - r_L^3\right) \mathrm{d}r' \tag{A12}$$

Substituting $r' = r_E - z'$ and $r_L = r_E - L$, we have

$$\frac{1}{3}\left(r'^3 - r_L^3\right) = \frac{1}{3}\left((r_E - z')^3 - (r_E - L)^3\right) \tag{A13}$$

$$= r_E^2(L - z') - r_E(L^2 - z'^2) + \frac{1}{3}(L^3 - z'^3) \tag{A14}$$

$$= r_E^2(L - z')\left[1 - \frac{1}{r_E}(L + z') + \frac{1}{3r_E^2}(L^2 + Lz' + z'^2)\right] \tag{A15}$$

where r_E is the constant radius of the Earth and L is the depth to the base of the lithosphere. Eq. (A15), therefore, provides the magnitude of error in GPE introduced by the flat-Earth approximation.

Let us denote GPE with the correct level of reference at the base of the lithosphere as $\bar{\sigma}_{zz}^{base}$ (eq. 7 in text), and let GPE with the sea level or geoid as reference level be $\bar{\sigma}_{zz}^{geoid}$ (eq. 8 in text). From eqs (7) and (8),

$$\bar{\sigma}_{zz}^{geoid} = \bar{\sigma}_{zz}^{base} + L \int_{-h}^{L} \rho(z) g \mathrm{d}z, \tag{A16}$$

which in spherical coordinates can be written as

$$\int_{r_L}^{r_0} r^2 \sigma_{rr} \mathrm{d}r + \int_{r_L}^{r_E} r^2 P_L \mathrm{d}r = -\int_{r_L}^{r_0} \frac{1}{3} \rho g \left(r^3 - r_L^3\right) \mathrm{d}r + \int_{r_L}^{r_0} \frac{1}{3} \rho g \left(r_E^3 - r_L^3\right) \mathrm{d}r \tag{A17}$$

$$= \int_{r_L}^{r_0} \frac{1}{3} \rho g \left(r_E^3 - r^3\right) \mathrm{d}r \tag{A18}$$

$$\frac{1}{3}\left(r_E^3 - r^3\right) = \frac{1}{3}\left(r_E^3 - (r_E - z)^3\right) = r_E^2 z - r_E z^2 + \frac{1}{3} z^3 \tag{A19}$$

where $P_L = \int_{r_L}^{r_0} \rho g \mathrm{d}r$, is the pressure at the base of the lithosphere. The first term on the left-hand side of (A17) is the GPE term in (A12).

The I functional in eq. (9) is given by

$$\begin{aligned} I = & \iint \frac{1}{\mu}\left[\bar{\tau}_{\phi\phi}^2 + 2\bar{\tau}_{\phi\theta}^2 + \bar{\tau}_{\theta\theta}^2 + (\bar{\tau}_{\phi\phi} + \bar{\tau}_{\theta\theta})^2\right] \cos\theta \, \mathrm{d}\phi \, \mathrm{d}\theta \\ & + \iint \left\{2\lambda_\phi \left[\frac{1}{\cos\theta} \frac{\partial \bar{\tau}_{\phi\phi}}{\partial \phi} + \frac{1}{\cos\theta} \frac{\partial}{\partial \phi}(\bar{\tau}_{\phi\phi} + \bar{\tau}_{\theta\theta}) + \frac{1}{\cos^2\theta} \frac{\partial}{\partial \theta}(\cos^2\theta \, \bar{\tau}_{\phi\theta}) + \frac{1}{\cos\theta} \frac{\partial}{\partial \phi} \bar{\sigma}_{rr}\right] \right. \\ & \left. + 2\lambda_\theta \left[\frac{1}{\cos\theta} \frac{\partial}{\partial \phi} \bar{\tau}_{\phi\theta} + \frac{3}{2} \frac{\partial}{\partial \theta}(\bar{\tau}_{\theta\theta} + \bar{\tau}_{\phi\phi}) + \frac{1}{2\cos^2\theta} \frac{\partial}{\partial \theta}(\cos^2\theta [\bar{\tau}_{\theta\theta} - \bar{\tau}_{\phi\phi}]) + \frac{\partial \bar{\sigma}_{rr}}{\partial \theta}\right]\right\} \cos\theta \, \mathrm{d}\phi \mathrm{d}\theta \end{aligned} \tag{A20}$$

where $\bar{\tau}_{ij}$ are the vertically integrated deviatoric stresses, $\bar{\sigma}_{rr}$ is the vertically integrated vertical stress, or GPE, λ_ϕ, λ_θ represent the horizontal components of the Lagrange multipliers, and μ is the relative viscosity.

The J functional in eq. (13) can be written in spherical coordinates as

$$J = \iint \left\{\left[\begin{pmatrix} \bar{\tau}_{\phi\phi} \\ \bar{\tau}_{\theta\theta} \\ \bar{\tau}_{\phi\theta} \end{pmatrix} - \begin{pmatrix} \Phi_{\phi\phi}^{\mathrm{obs}} \\ \Phi_{\theta\theta}^{\mathrm{obs}} \\ \Phi_{\phi\theta}^{\mathrm{obs}} \end{pmatrix}\right]^T \widetilde{V}^{-1} \left[\begin{pmatrix} \bar{\tau}_{\phi\phi} \\ \bar{\tau}_{\theta\theta} \\ \bar{\tau}_{\phi\theta} \end{pmatrix} - \begin{pmatrix} \Phi_{\phi\phi}^{\mathrm{obs}} \\ \Phi_{\theta\theta}^{\mathrm{obs}} \\ \Phi_{\phi\theta}^{\mathrm{obs}} \end{pmatrix}\right]\right\} \cos\theta \, \mathrm{d}\phi \, \mathrm{d}\theta \tag{A21}$$

where

$$\bar{\tau}_{\phi\phi} = \mu\left(\frac{1}{\cos\theta} \frac{\partial \lambda_\phi}{\partial \phi} - \lambda_\theta \tan\theta\right), \tag{A22}$$

$$\bar{\tau}_{\theta\theta} = \mu \frac{\partial \lambda_\theta}{\partial \theta}, \tag{A23}$$

$$\bar{\tau}_{\phi\theta} = \frac{\mu}{2}\left(\frac{\partial\lambda_\phi}{\partial\theta} + \frac{1}{\cos\theta}\frac{\partial\lambda_\theta}{\partial\phi} + \lambda_\phi \tan\theta\right), \tag{A24}$$

$$\tilde{\mathbf{V}}^{-1} = \frac{1}{\mu}\begin{pmatrix} 2 & 1 & 0 \\ 1 & 2 & 0 \\ 0 & 0 & 2 \end{pmatrix} \tag{A25}$$

and

$$(\Phi^{\rm obs}_{\phi\phi}, \Phi^{\rm obs}_{\theta\theta}, \Phi^{\rm obs}_{\phi\theta})^T = \left(-\frac{\bar{\sigma}_{rr}}{3}, -\frac{\bar{\sigma}_{rr}}{3}, 0\right)^T. \tag{A26}$$

The relation between 2-D and 3-D stresses (eqs 24–26 in text) is given by

$$\bar{\tau}^{2D}_{\theta\theta} = 2\bar{\tau}^{3D}_{\theta\theta} + \bar{\tau}^{3D}_{\phi\phi} \tag{A27}$$

$$\bar{\tau}^{2D}_{\phi\phi} = \bar{\tau}^{3D}_{\theta\theta} + 2\bar{\tau}^{3D}_{\phi\phi} \tag{A28}$$

$$\bar{\tau}^{2D}_{\phi\theta} = \bar{\tau}^{3D}_{\phi\theta}. \tag{A29}$$

APPENDIX B: DYNAMIC TOPOGRAPHY

Dynamic topography is defined as the topography that arises from sub-lithospheric density anomalies, which drive mantle flow. The radial component of mantle flow (τ_{rr}) causes vertical displacements of the lithosphere producing dynamic topography. These kinds of topographical features are in contrast to those created by density variations within the lithosphere that might be called static topography. The total topography that we observe on the surface of the Earth is the net sum of these static and dynamic parts. Isolation of this dynamic topography provides a constraint on the lithospheric contribution of topography. Thus, one aim of our study is to distinguish between these two types of topographies by estimating the styles and magnitudes of dynamic topography from our crustal solutions. Estimates of global dynamic topography have been provided by Hager *et al.* (1985), Cazenave *et al.* (1989), Panasyuk & Hager (2000), Steinberger *et al.* (2001), Steinberger (2007) and Lithgow-Bertelloni & Guynn (2004). Cazenave *et al.* (1989) and Panasyuk & Hager (2000) calculated dynamic topography by removing the effects of isostatic topography from the observed topography, the same way as we do here. Steinberger *et al.* (2001) and Lithgow-Bertelloni & Guynn (2004) used mantle flow field whereas Hager *et al.* (1985) used geoid anomalies to calculate dynamically induced topography.

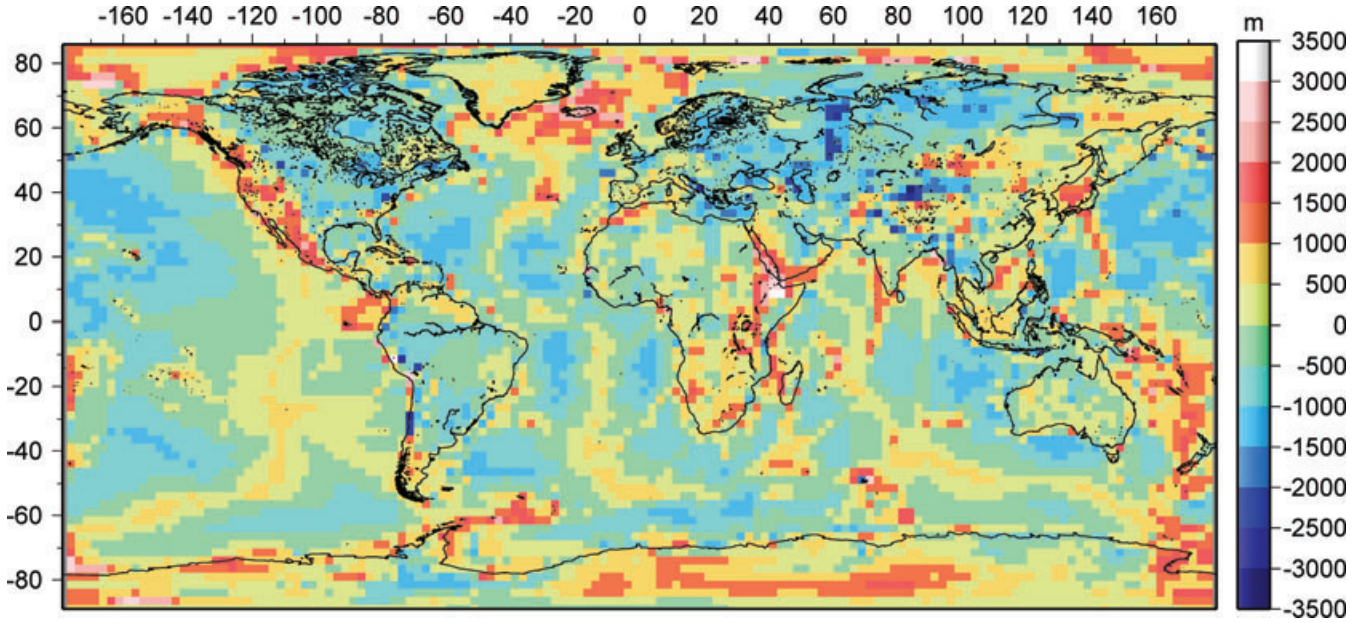

Figure B1. Global distribution of dynamic topography. The white and red areas indicate positive dynamic topography whereas the blue areas indicate negative dynamic topography. The maximum dynamic topography ∼3.5 km occurs in Central East Africa. Topography on scalebar is in metres.

GPE values from the uncompensated model contain the influence of dynamic topography as well. The weight of the lithospheric column, $\sigma_{zz}(L)$, at reference depth L is given by $\sigma_{zz}(L) = \int_{-h}^{L} \rho(z')g(z')dz' = \sigma^{\circ}_{zz}(L) + \tau_{zz}(L)$, in the presence of dynamic topography. This formulation ignores any contribution from flexure. Here, $\sigma^{\circ}{}_{zz}(L)$ is the reference stress, whereas $\tau_{zz}(L)$ is the radial traction at reference level L associated with deeper mantle flow that is responsible for producing dynamic topography. To remove the dynamic topography contribution, an isostatically compensated solution (uniform vertical stress at depth L) is calculated. One way of compensating our solution, as stated before, is by adjusting the elevations of the crustal blocks. Accordingly, areas with lower than average vertical stress at reference depth L get elevated to achieve uniform vertical stress at reference level whereas those with higher than average vertical stress at depth L are lowered in elevation. Thus, the difference between the compensated topography and observed topography should provide an estimate of the magnitude of dynamic topography. In our model, the highest magnitude dynamic topography (∼3.5 km) occurs in eastern Africa (Fig. B1) (Lithgow-Bertelloni & Silver 1998). Other areas of positive dynamic topography are Northern Atlantic near Greenland and parts of western North America. Somewhat lower magnitude positive dynamic topography occurs along the mid-oceanic ridges. These are possible areas of upwelling, whereas areas of negative dynamic topography include eastern North America, parts of western Europe, and the deeper oceans. Our results bear considerable similarities to that of Panasyuk & Hager (2000) who computed dynamic topography in the above procedure; the only difference is that they used a less fine crustal data set than we have. There might be possible errors in our estimates of dynamic topography magnitudes due to uncertainties in the upper-mantle densities. However, this will not have any considerable effect on the styles of dynamic topography.

APPENDIX C

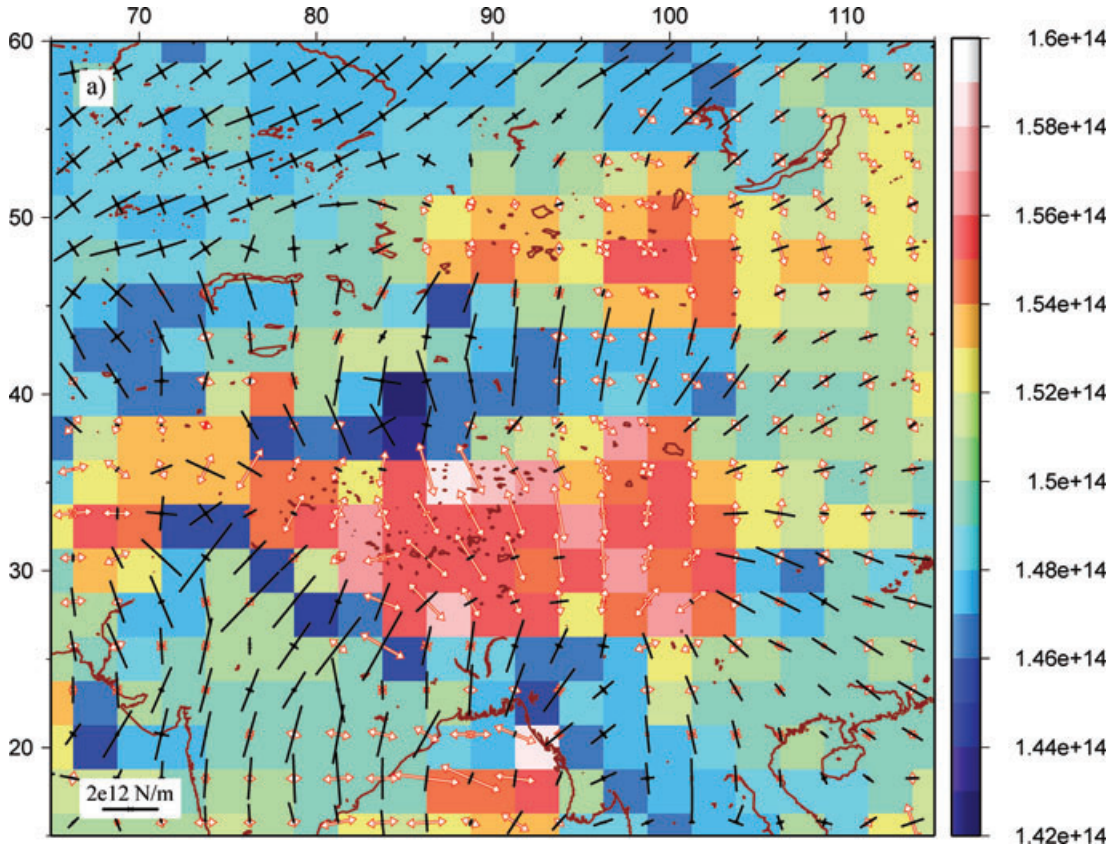

Figure C1. Same as Fig. 2 with (a) Asia, (b) North America, (c) the Aegean region, (d) the Central Indian Ocean and (e) eastern Africa zoomed in.

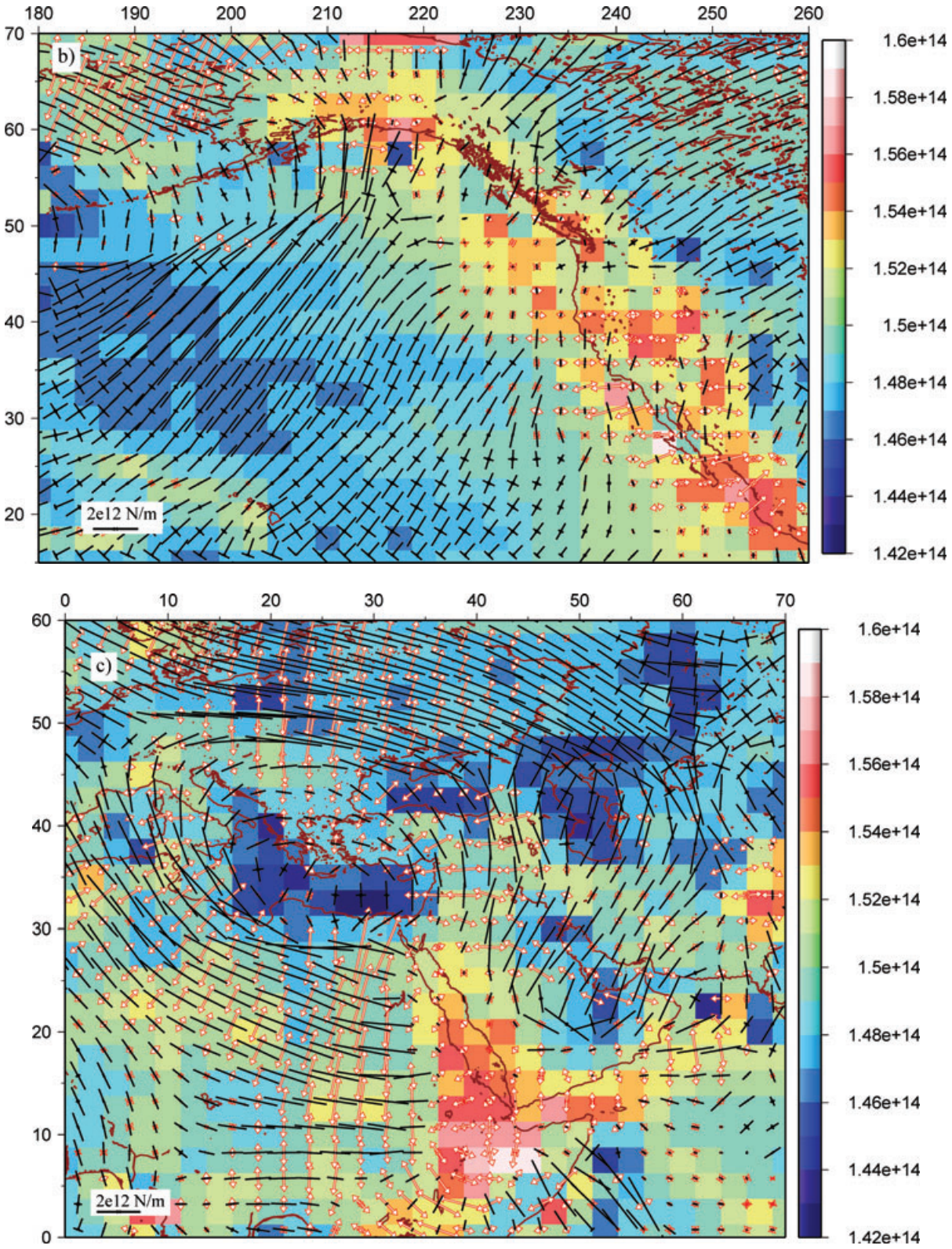

Figure C1. (*Continued.*)

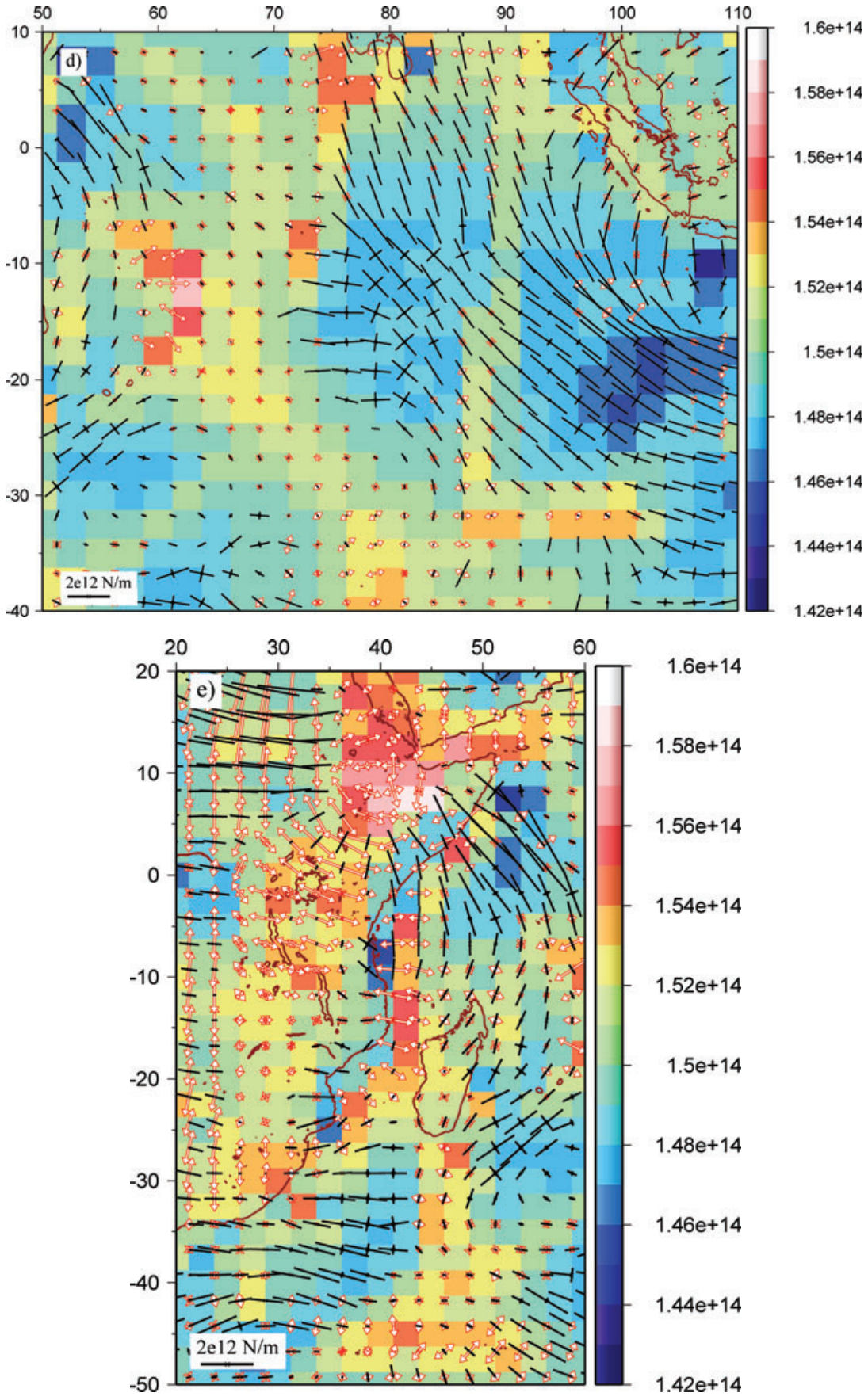

Figure C1. (*Continued.*)

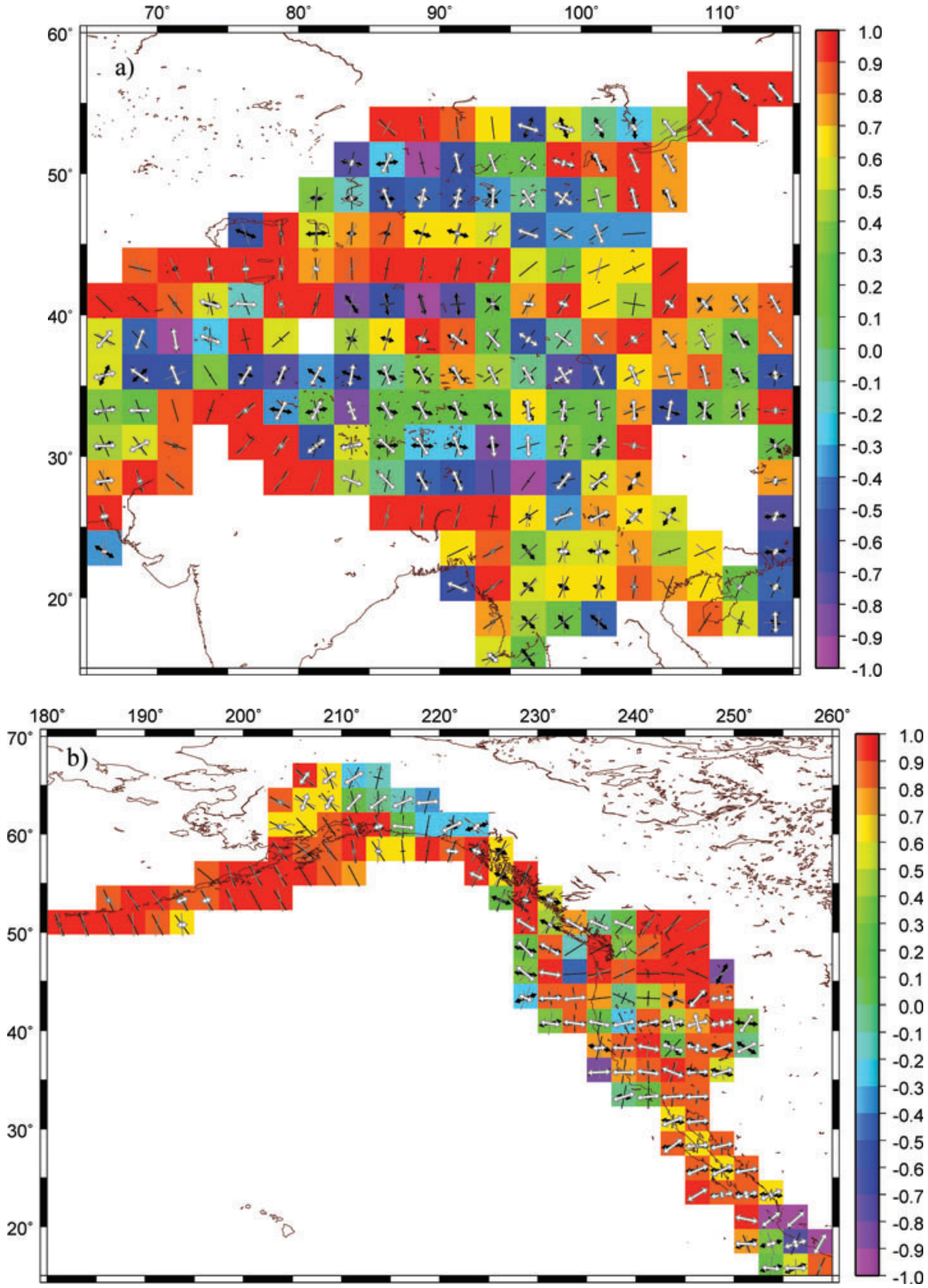

Figure C2. Same as Fig. 9 with (a) Asia, (b) North America, (c) the Aegean region, (d) Central Indian Ocean and (e) Africa zoomed in and the unit tensors shown on top of the correlation. Thick, clear arrows with grey outline are tensional axes of the predicted deviatoric stress tensors (unit tensor), whereas thin grey arrows are the compressional axes of the predicted deviatoric stress tensors. Black denote the strain rate unit tensors. Thick black arrows are extensional strain rate axes, thin black arrows are compressional.

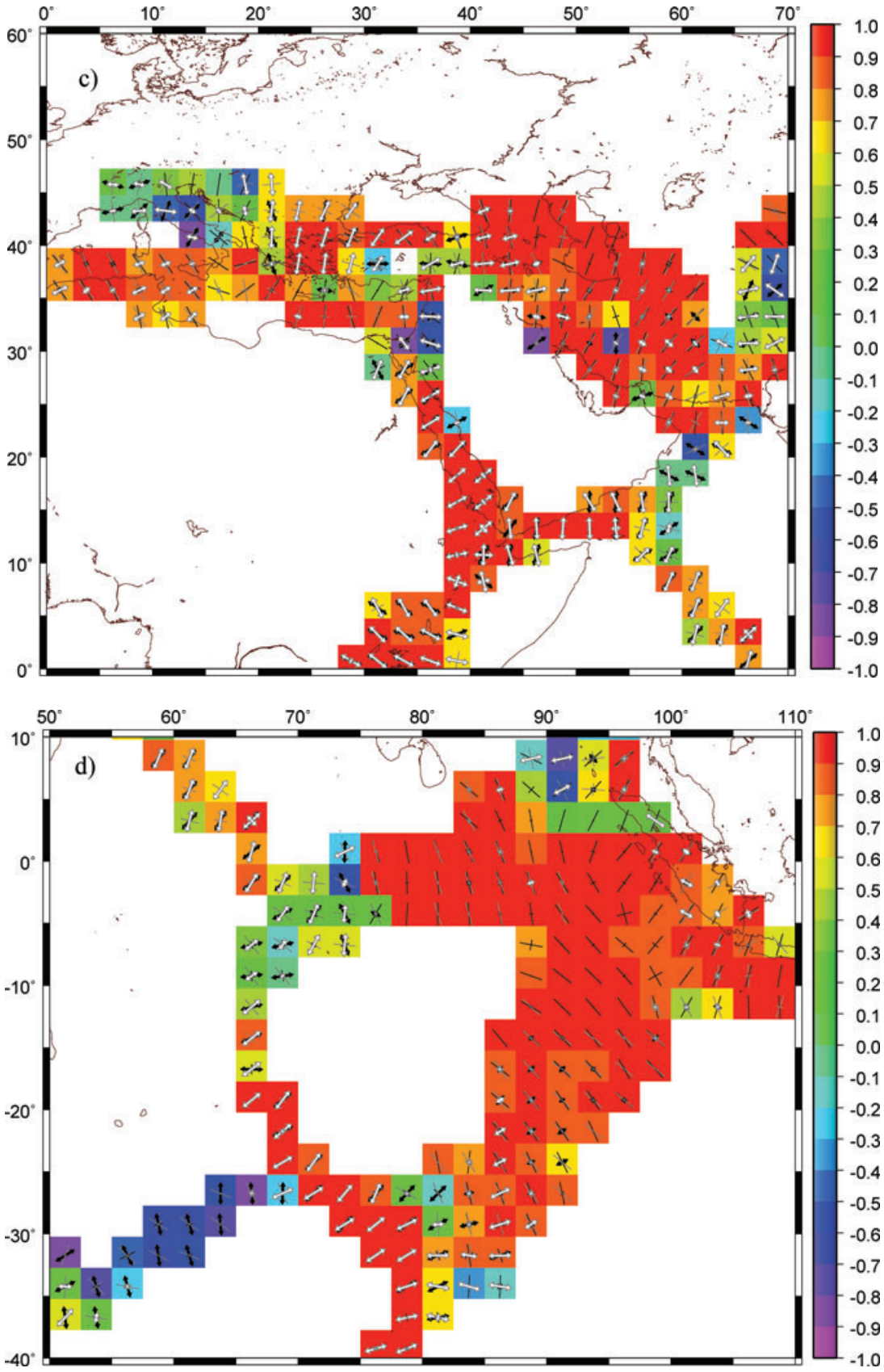

Figure C2. (*Continued.*)

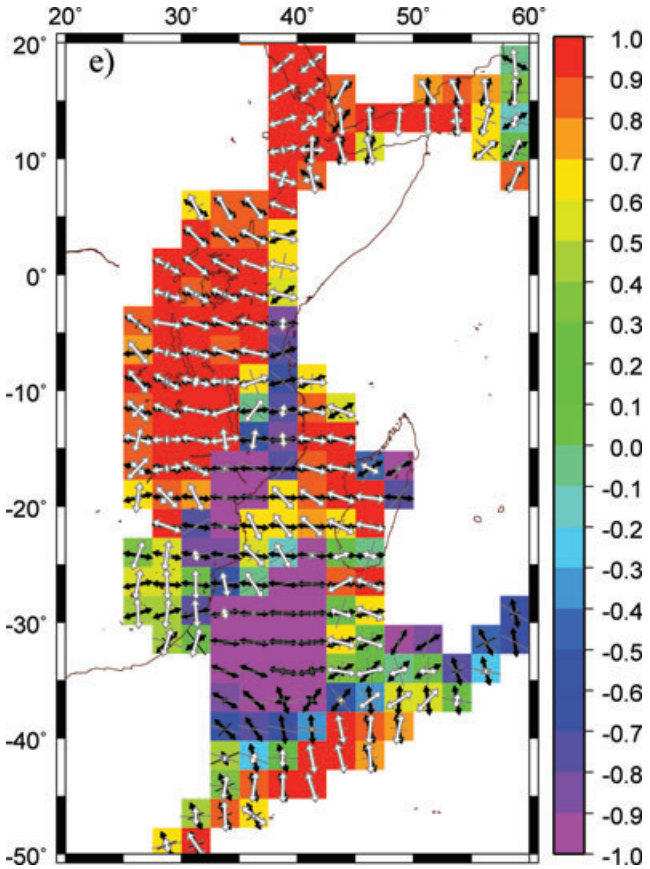

Figure C2. (*Continued.*)